scientific reports

Check for updates

OPEN

In silico analysis of patient specific coagulation and flow effects on fibrin clot formation

J. M. H. Cruts[1], M. Rezaeimoghaddam[2], A. Rachid[2], L. Bontempi[1], R. A. Arisz[3], F. N. van de Vosse[2] & F. J. H. Gijsen[1,4]✉

The coagulation cascade, triggered by tissue factor (TF) exposure after endothelial injury, drives fibrin formation and may result in thrombotic events such as stroke. The mechanisms driving differences in thrombus extent among patients remain poorly understood, but interactions between patient-specific coagulation and local blood flow are thought to be critical. This study presents a unified workflow with an assay-calibrated, experimentally validated in silico model that links coagulation assays to flow-resolved simulations in patient-specific geometries. Plasma from ischemic stroke patients was analyzed with a thrombin generation (TG) assay, and a 0D computational model was fitted to TG curves to infer patient-specific coagulation parameters. These parameters were validated against thrombodynamics (TD) outcomes using 1D computational reaction–diffusion simulations. The framework was extended to 2D computational flow domains to assess the influence of shear rate, TF patch size and location, and geometric features such as stenosis. Finally, 3D carotid simulations combined patient-specific vascular geometries with plasma parameters. The 0D model reproduced TG data, while 1D simulations matched TD outcomes for clot size, fibrin growth, and thrombin wave speed. In 2D, fibrin formation was reduced at higher shear or smaller TF patches, and 3D simulations demonstrated the combined effect of flow, geometry, and plasma composition on fibrin formation. This approach provides a bridge from bench assays to hemodynamic contexts and offers a potential path toward individualized thrombotic risk assessment.

Keywords Fibrin, Coagulation, Computational fluid dynamics, Patient-specific, In silico, Clot

Thrombosis is the formation of blood clots within blood vessels, which is a tightly controlled process governed by the coagulation cascade. When a vessel wall is damaged, exposure of tissue factor (TF) from the subendothelium activates the extrinsic pathway of coagulation. This involves a chain of biochemical reactions which activate the primary coagulation factor thrombin, and ultimately results in the formation of a fibrin network[1]. Together with platelets and red blood cells, this forms an insoluble clot that normally prevents bleeding, but excessive clot formation can obstruct blood flow and cause ischemic events such as stroke[2,3]. Carotid artery stenosis poses a significant risk of stroke[4]. When the vulnerable atherosclerotic plaque ruptures, the lipid core including TF-expressing microparticles becomes exposed to the blood's thrombogenic factors and a clot will be formed, a process called atherothrombosis. Clots in ruptured plaques have been reported to be primarily fibrin and/or red blood cell (RBC) rich[2,3,5]. This is believed to be caused by, amongst others, the abundance of TF within the plaques and recirculation zones immediately distal to the plaque[5–8].

The degree of atherothrombosis varies widely and only a minority of plaque ruptures results in noticeable symptoms, while others heal silently and form only mural thrombus[2,4]. It is thought that this is related to an increased coagulability[9], although studies show conflicting results on for example the association between plasma factors and the risk of ischemic stroke[10,11]. Nevertheless, these studies did not investigate the effects of flow, which is known to have a significant impact on coagulation dynamics and the fibrin structure[12–15]. Our understanding of how fibrin formation in combination with flow effects influences the magnitude of the thrombotic response remains incomplete[16,17]. It is hypothesized that there is a synergistic effect on the degree of atherothrombosis between the variability in coagulations factors among individuals and altered hemodynamics. Although in vivo mouse experiments[18] and in vitro micro-fluidic setups[19,20] are promising in investigating this

[1]Department of Biomedical Engineering, Erasmus Medical Center, Rotterdam, The Netherlands. [2]Department of Biomedical Engineering, Eindhoven University of Technology, Eindhoven, The Netherlands. [3]Department of Hematology, Cardiovascular Institute, Erasmus Medical Center, Rotterdam, The Netherlands. [4]Department of Biomechanical Engineering, Delft University of Technology, Delft, The Netherlands. ✉email: f.j.h.gijsen@tudelft.nl

matter, these approaches can be extremely time-consuming and expensive, and they suffer from translational challenges.

Computational modeling has emerged as a potent tool for investigating how fibrin clots form under the influence of blood flow[21–23]. Numerous models have already been developed to simulate the formation of the fibrin clot including 0D ordinary differential equation (ODE) systems[24–26], 1D reaction-diffusion models[27–31], and 2D and 3D convection-diffusion models[1,13,16,17,32–34]. One of the benefits of using these models is that they can overcome limitations of in vitro and in vivo experiments[28]. However, despite substantial advances in mathematical and computational modeling of fibrin formation, achieving a comprehensive quantitative model of the process remains a significant challenge[35–37]. Moreover, existing computational models that seem to capture the formation of a fibrin network reasonably often contain numerous equations and are computationally expensive[38]. As a result, their direct application to large-scale or patient-specific 3D geometries is challenging.

Furthermore, the composition of blood plasma, including coagulation factors, can vary significantly among individuals. This can lead to spatial and temporal variations in coagulation dynamics[28,39–41]. Currently available computational models of fibrin formation often fail to account for individual variations in blood plasma composition, therefore neglecting potential complications such as accelerated fibrin growth in thrombotic plasma. The majority of the 0D models aiming to capture the coagulation cascade contain kinetic constants that are fixed as input[42]. Moreover, most previously developed models did not take into account the varying composition of blood plasma for validation purposes or even completely lacked direct comparison to in vitro experiments.

We propose a workflow (see Fig. 1) in which we combine an in silico continuum model of injury-induced patient-specific coagulation, that accurately captures the variability in spatio-temporal dynamics of thrombin and fibrin, and use this model to investigate the effects of hemodynamics on fibrin formation. We build on the model of Ratto et al. (2021)[33,43] and adapt it to our purposes. First, we infer patient-specific coagulation parameters by fitting the 0D in silico model to in vitro thrombin generation (TG) curves from ischemic stroke patients. TG is a widely used, gold standard method to measure TG and coagulation potential. Next, we embed

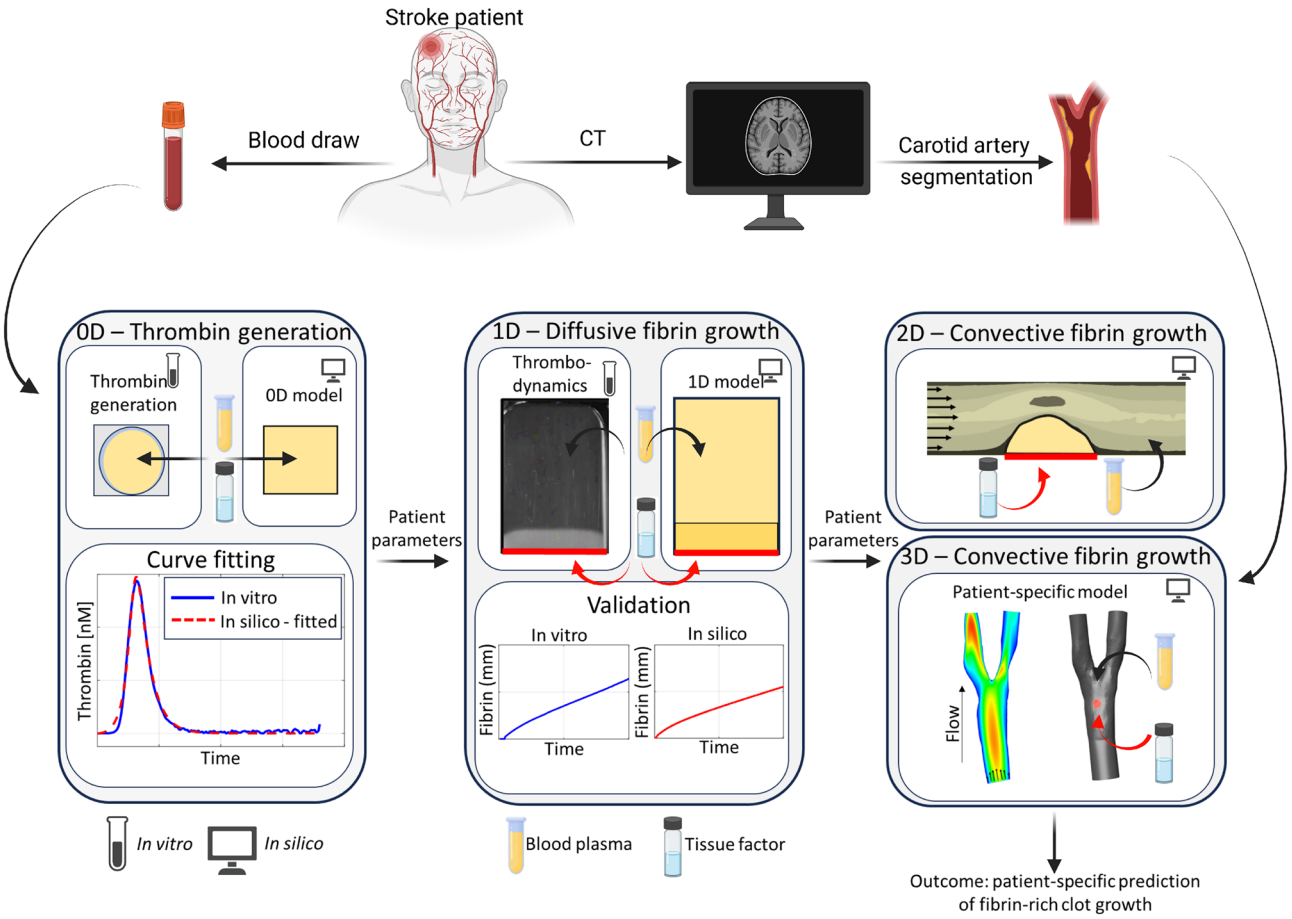

Fig. 1. General workflow of the current study. The workflow integrates patient-specific carotid artery segmentations and corresponding blood data (top). Left panel: 0D in vitro and in silico thrombin generation (TG), with in silico curve fitting to the in vitro TG data. Middle panel: 1D in vitro thrombodynamics (TD) and 1D in silico modeling, validated by comparing the resulting fibrin formation curves. Right panel: Fibrin growth under flow, simulated in 2D within a straight channel (top) and in 3D within a patient-specific carotid artery geometry (bottom).

these parameters in a larger in silico 1D reaction-diffusion model and validate it with in vitro thrombodynamics (TD) data from the same cohort. TD is a relatively new assay that records the spatio-temporal propagation of coagulation and visualizes fibrin clot formation. Then, we implement the validated model in 2D in silico flow simulations, with which the effect of flow phenomena like recirculation zones and varying shear rate, and varying geometrical features like a backward-phasing step (BFS) and stenosed area, will be investigated. Finally, a 3D case will demonstrate fibrin clot formation in realistic patient-specific geometries with patient-specific blood data. Our aim is to use this model to improve our understanding of the mechanisms underlying the combined effect of patient-specific coagulation and flow, and gain more knowledge on the causes of varying degrees of atherothrombosis.

Methods

Workflow

The workflow is visualized in Fig. 1, which will be described in more detail in the next sections. In brief, first, in vitro TG curves were obtained. The TG test analyses the amount of thrombin being formed in time in a certain amount of blood plasma after coagulation activation with TF[44]. Next, a biophysical model of a fibrin clot formation is developed. This model employs a reduced 0D coagulation model that solves for the concentrations over time of factor Xa, prothrombin, and thrombin. Patient-specific parameters are determined through curve fitting against the in vitro TG test data. Subsequently, these parameters are integrated into a 1D in silico model, including a system of coupled reaction-diffusion equations, additionally solving for fibrinogen and fibrin concentrations. In this 1D model, the bottom wall represents a TF coated surface, initiating coagulation. The in silico spatio-temporal dynamics of thrombin and fibrin are tracked and compared with results of the in vitro TD assay, which is performed with the same plasma as the TG test. Finally, the validated 1D model is implemented in a 2D geometry, representing a blood vessel. In this geometry, the TF represents vessel wall injury, which subsequently will initiate coagulation. Flow is applied, representing the blood flow. This setup is used to investigate the effect of varying flow conditions in combination with patient-specific plasma, and is applied in a stenosed geometry to compare proximal versus distal clot formation. Finally, the model is implemented in patient-specific geometries of patients with a stenosed carotid artery to demonstrate potential future applications.

0D Methods

0D In silico model

The first step in the workflow is to mimic clinical TG test data using a simplified mathematical model of blood coagulation developed by Ratto et al.[43,45]. This reduced model was derived from a more comprehensive model proposed by Panteleev et al.[46]. Ratto et al. reduced the original system of 17 equations to a system of 3 equations, given in Table 1. Here, X_a is the concentration over time of the clotting factor Xa, involved in the initiation phase, and X_0 is its unactivated form. P and T are prothrombin and thrombin, respectively. The parameters k_1 - k_9 are expressed through the parameters of the extensive model of Panteleev et al. (2010)[46]. The currently adapted model is visualized in Fig. 2. Each parameter corresponds to a biological role. Parameter k_1 defines the initiation of the coagulation by TF, which activates factor X_0. Parameters k_2 and k_3 represent a positive feedback loop, which also activate factor X_0. Factor Xa is being inhibited by the TF pathway inhibitor, which corresponds to parameter k_4. Parameter k_5 describes the transformation of prothrombin into thrombin, catalyzed by factor Xa. Parameters k_6, k_7, and k_8 reflect the three feedback loop mechanisms within this system, capturing the activation of factors V, VIII, and XI. This feedback loop drives a self-sustaining cycle of thrombin generation, which occurs when the amount of thrombin generated during the initiation phase exceeds a certain threshold. The generation of thrombin is being inhibited by antithrombin, which corresponds to parameter k_9. The 0D system was solved in MATLAB (The MathWorks, Inc., Natick, MA, USA; version R2021b; https://www.mathworks.com/) using a first-order explicit (forward) Euler method with a fixed time step of 0.01 s. Each simulation was run for 60 min to match the time-frame of the TG experiments.

0D In silico curve fitting

The 0D coagulation model (Table 1) is calibrated by adjusting the most significant parameters, determined by sensitivity analyis, in order to minimize the difference between the numerical prediction and experimental observations of the TG curve. The acquisition of experimental observations will be described in the next section. Sensitivity analysis is performed to identify which input parameters ($k1 - k9$) of the 0D coagulation model have the most significant impact on the output TG curve.

The used approach is an adaptive generalised polynomial chaos expansion (gPCE) method[47,48]. More detailed information on this method and its current application can be found in Supplementary Information S1. In brief, the gPCE method creates a meta-model, in which Sobol sensitivity indices of the input parameters are

Variable	Governing equation
X_a	$\frac{dX_a}{dt} = (k_1 + k_2\,T + k_3\,T^2)\,(X_0 - X_a) - k_4\,X_a$
P	$\frac{dP}{dt} = -\,(k_5\,X_a + k_6\,T + k_7\,T^2 + k_8\,T^3)\,P$
T	$\frac{dT}{dt} = (k_5\,X_a + k_6\,T + k_7\,T^2 + k_8\,T^3)\,P - k_9\,T$

Table 1. System of ordinary differential equations governing the evolution of activated factor X_a, prothrombin P, and thrombin T, from Ratto et al.[45].

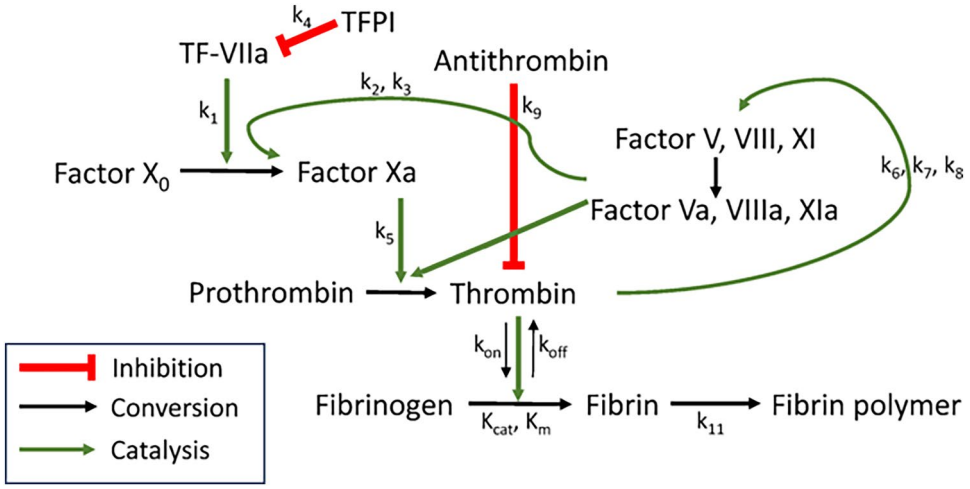

Fig. 2. Modeled coagulation cascade with incorporated coagulation factors and reaction rates. Conversion, catalysis, and inhibition are indicated with black, green, and red arrows, respectively. TF = tissue factor, TFPI = tissue factor pathway inhibitor. The model is partially adopted from Ratto et al. and Chatterjee et al.[26,43].

computed, which represent the contribution of each parameter to the variance of the output parameter. In our case, the input parameters are $k1 - k9$, and the output parameters are pre-defined qualities of interest (QoIs), based on the TG curve. Parameters with a sensitivity index greater than 0.1 are considered significant[49]. From this method, it was concluded that the parameters $k1$, $k5$, $k8$, and $k9$ have the greatest influence on the TG curve (Supplementary Fig. S1).

The method of model calibration is described in detail in Supplementary Information S2, and an overview of the steps performed during the calibration procedure is shown in Supplementary Fig. S2. In brief, a curve fitting method in MATLAB R2021b is applied to each patient-specific in vitro TG curve. The used approach is the nonlinear least squares method, which iteratively adjusts parameter values to minimize an objective function. This function is expressed as the sum of squared residuals representing the difference between observed data (in vitro TG curve) and model predictions (in silico TG curve). The most significant parameters ($k1$, $k5$, $k8$, and $k9$) are calibrated, while others are set fixed based on the original parameters described by Ratto et al. (2021)[45].

0D In vitro data

Platelet-poor plasma (PPP) samples were obtained as part of the PARISK (Plaque At RISK) study[50], a prospective, multicenter cohort study including patients who had a mild-to-moderate stenosis in the carotid artery and who had a recent transient ischemic attack (TIA) or minor stroke. The study was approved by the Medical Ethics Committee of Maastricht University Medical Center+ and Maastricht University (approval number NL29116.068.09/MEC 09-2-082), and all individuals provided written informed consent. This study was conducted in accordance with all relevant guidelines and regulations for research involving human participants and adhered to the principles of the Declaration of Helsinki. All samples were previously analyzed for TG, of which all available samples at Erasmus Medical Center, Rotterdam (N=54) are used in the current study[51]. In brief, citrated PPP samples were obtained from baseline blood draws. TG was performed using the calibrated automated thrombogram (CAT; Thrombinoscope BV, Maastricht, The Netherlands), a validated assay method[44]. Each reaction used 80 µL of PPP with 1 pM TF and phospholipids. Additional methodological details are described by Crombag et al.[51].

0D Data analysis

From each TG curve, the following QoIs were extracted: the peak height (p_h: maximum thrombin concentration), time to peak (T_{tp}: time to reach maximum thrombin concentration), endogenous thrombus potential (*ETP*: total amount of thrombin generated) and lag time (T_{lag}: time until TG starts), see Fig. 3A.

1D Methods

1D In silico model

The previously described 0D coagulation model is extended to 1D by taking diffusion of the coagulation factors into account. The previously described ODE system (Table 1) and its corresponding patient-specific fitted parameters are used as an input for the 1D model. Additionally, the conversion of fibrinogen into fibrin (monomers), and its coupling with thrombin are implemented (see Fig. 2). The equations for this system are adapted from the comprehensive model of Chatterjee et al.[26]. We retain only the core reactions that govern the primary fibrin monomer formation by thrombin cleavage of fibrinogen and reversible complex formation. In the original work of Chatterjee et al.[26], thrombin (T) cleaves fibrinogen (F_g) into fibrin monomers (F) via the elementary enzyme–substrate mechanism

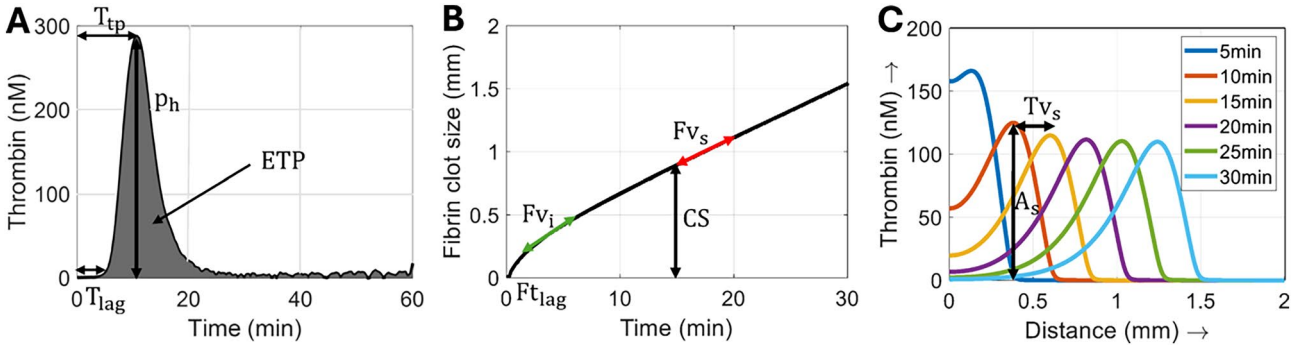

Fig. 3. Variables for thrombin generation (TG) and thrombodynamics (TD). (**A**) TG, with the peak height (p_h), time to peak (T_{tp}), endogenous thrombus potential (*ETP*), and lag time (T_{lag}), (**B**) TD fibrin clot growth, with fibrin lag-time (Ft_{lag}), the initial rate of clot growth (Fv_i), stationary rate of clot growth (Fv_s) and clot size (*CS*), and (**C**) TD thrombin spatio-temporal dynamics, with the amplitude of the thrombin peak (A_{st}), and the rate of thrombin peak propagation (Tv_s).

Variable	Governing equation
X_a	$\frac{dX_a}{dt} - D_{X_a}\,\frac{\partial^2 X_a}{\partial x^2} = (k_2\,T + k_3\,T^2)\,(X_0 - X_a) - k_4\,X_a$
P	$\frac{dP}{dt} - D_P\,\frac{\partial^2 P}{\partial x^2} = -\,(k_5\,X_a + k_6\,T + k_7\,T^2 + k_8\,T^3)\,P$
T	$\frac{\partial T}{\partial t} - D_T\,\frac{\partial^2 T}{\partial x^2} = \begin{array}{r}(k_5\,X_a + k_6\,T + k_7\,T^2 + k_8\,T^3)\,P \\ -\,k_9\,T - k_{\rm on}\,T\,F_g + \frac{k_{\rm off} + k_{\rm cat}}{K_m}\,T\,F_g\end{array}$
F_g	$\frac{\partial F_g}{\partial t} - D_{F_g}\,\frac{\partial^2 F_g}{\partial x^2} = -\,k_{\rm on}\,T\,F_g + \frac{k_{\rm off}}{K_m}\,T\,F_g$
F	$\frac{\partial F}{\partial t} - D_F\,\frac{\partial^2 F}{\partial x^2} = \frac{k_{\rm cat}}{K_m}\,T\,F_g - k_{11}\,F$
F_P	$\frac{\partial F_P}{\partial t} = k_{11}\,F$

Table 2. System of partial differential equations governing the evolution of activated factor X_a, prothrombin P, thrombin T, fibrinogen F_g, fibrin F, and fibrin polymer F_P.

$$T + F_g \underset{k_{\rm off}}{\overset{k_{\rm on}}{\rightleftarrows}} [T:F_g] \xrightarrow{k_{\rm cat}} T + F,$$

where $[T{:}F_g]$ represents the thrombin-fibrinogen complex. The associated mass–action terms in the species balances are

$$\frac{\partial [T:F_g]}{\partial t} = k_{\rm on} T F_g - (k_{\rm off} + k_{\rm cat})[T:F_g], \quad \frac{\partial F_g}{\partial t} = -k_{\rm on} T F_g + k_{\rm off}[T:F_g],$$
$$\frac{\partial F}{\partial t} = k_{\rm cat}[T:F_g], \quad \frac{\partial T}{\partial t} = -k_{\rm on} T F_g + (k_{\rm off} + k_{\rm cat})[T:F_g],$$

where $k_{\rm on}\,TF_g$ represents the rate of thrombin binding to fibrinogen , $k_{\rm cat}[T:F_g]$ represents the rate of fibrinogen conversion to fibrin by thrombin , and $k_{\rm off}[T:F_g]$ represents the regeneration of free thrombin and fibrinogen. Explicitly evolving $[T:F_g]$ increases computational cost in the reaction–diffusion system, hence we adopt the standard Michaelis–Menten reduction[52], applied here in a linearized form. Defining $K_M = (k_{\rm off} + k_{\rm cat})/k_{\rm on}$, and applying the quasi–steady-state approximation for the complex, we replace $[T:F_g]$ by $[T:F_g] \approx \frac{T\,F_g}{K_M}$. This relation is then substituted into the mass–action terms. The full set of reaction–diffusion equations for T, F_g, and F, together with the equations for the other coagulation factors, is given in Table 2.

The term $k_{11}F$ represents the simplified conversion of fibrin into fibrin polymer[33]. Since fibrin polymer F_p forms a solid clot, it does not diffuse. An overview of the used parameter values is shown in Table 3. Parameters k_{on}, k_{cat}, k_{off}, and K_m are taken from Chatterjee et al.[26]. Based on a preliminary dataset of normal pooled plasma (NPP) for which both TG and thrombodynamics measurements were available, we performed an assay-bridging calibration of the thrombodynamics parameter k_{cat}, adjusting it from 84 to 83 (see Supplementary Information S3 for more details). This adjustment slows the coagulation conversion dynamics and improves

Reaction rate	Value	Unit	Reference
k_{on}	0.1	$\mathrm{nM^{-1}s^{-1}}$	[26]
k_{off}	636	$\mathrm{s^{-1}}$	[26]
k_{cat}	83	$\mathrm{s^{-1}}$	[26] + calibration
K_m	7200	nM	[26]
k_{11}	0.1	$\mathrm{nM^{-1}s^{-1}}$	[33]
D	5×10^{-11}	$\mathrm{m^2s^{-1}}$	[33]
β_1	0.225	$\mathrm{nM^{-1}}$	[33]

Table 3. Parameter values used in the 1D model, with values taken from Chatterjee et al. and Bouchnita et al.[26,33].

Variable	Initial concentration [nM]	Diffusion coefficient $[\mathrm{m^2s^{-1}}]$
X_0	135	-
X_a	0	6.49×10^{-11}
P	1400	4.58×10^{-11}
T	0	5.69×10^{-11}
F_g	7000	2.73×10^{-11}
F	0	2.17×10^{-11}
F_p	0	-

Table 4. Concentrations at T=0 and diffusion coefficients. Initial concentrations are from Bouchnita et al.[33]. Diffusion coefficients are from Anand et al. and Bodnar et al.[53,54].

agreement of the predictive 1D model with in vitro thrombodynamics profiles. The calibrated value of k_{cat} was estimated once using the NPP dataset and subsequently applied uniformly to all simulations, without further tuning. Patient-specific variability is therefore captured exclusively through the CAT-fitted TG parameters.

Also, here and in what follows, D_i is the diffusion coefficient, taken specifically for each protein[53,54]. To match with the in vitro situation in the TD assays, all diffusion coefficients were corrected for plasma viscosity and temperature by multiplying by 0.88, as suggested by Dashkevich et al. [39]. The diffusion coefficients and initial concentrations are shown in Table 4.

The initiation of coagulation is simulated by applying a TF surface, and the spatio-temporal dynamics of thrombin and fibrin are measured. At one wall of the computational domain, a TF coated surface is represented by a prescribed flux of factor X_a, represented by the following boundary condition, adapted from Bouchnita et al.[33]:

$$\left.\frac{\partial X_a}{\partial \mathrm{n}}\right|_{x=0} = \frac{k_1 \left(X_0 - X_a\right)}{D\left(1 + \beta_1 \left(X_0 - X_a\right)\right)} \tag{1}$$

where β_1 is a constant, and D is taken as an average constant value for the diffusion coefficient. The difference with the original flux of Bouchnita et al.[33] is that α_1 (originally fitted based on experimental observations from Shen et al.[19]) is replaced by the patient-specific fitted parameter k_1. On the opposite side of the computational domain a zero-flux boundary condition is applied for factor X_a.

To solve for the 1D reaction-diffusion equations the Finite Difference Method is used. The numerical approach combines first-order upwind time discretization and second-order central difference implicit spatial discretization, and was implemented in a developed in-house code in MATLAB R2021b. The total simulated domain is 4 mm long, and an element size of 0.01 mm and a time step of 0.01 s were used, as determined from spatial and temporal sensitivity analyses. Each simulation is solved for 60 min, in order to match the time-frame of the performed TD experiments.

1D In vitro data

The TD assay is performed to monitor the propagation of thrombin and fibrin clot growth from a TF-coated surface (see Fig. 1, middle panel). This is performed on 20 pre-selected samples, with the same plasma as is used for the TG assays. The pre-selection is based on the area-under-the-curve (*ETP*) and the peak height (p_h) obtained from the TG assays (see Fig. 3A). Samples that contained an *ETP* and/or p_h in the upper- or lower inter-quartile range of all available samples at Erasmus Medical Center (N=54) were included. The general concept of the TD test was previously described by others[39]. In brief, coagulation is initiated in a thin layer of plasma upon contact with TF immobilized on a plastic substrate, thereby mimicking localized vascular injury. Fibrin clot formation is triggered at the TF-coated surface and subsequently propagates into the surrounding

TF-free plasma. The progression of fibrin formation is visualized through time-lapse imaging, based on the light-scattering properties of the fibrin network. Thrombin activity was monitored using a fluorogenic substrate containing 7-amino-4-methylcoumarin (AMC), which is specifically cleaved by thrombin. Upon enzymatic cleavage, free AMC is released into the plasma and becomes fluorescent, allowing quantification of thrombin generation kinetics. PPP is used with the PLS kit, according to the instructions of the TD manufacturer (HemaCore, Moscow, Russia). The plasma aliquots were stored at -80°C until analysis, and prior to testing, samples were thawed at 37°C for 5 min. The PPP was pre-treated with Corn Trypsin Inhibitor for 10 min at 37° C. Images of clot growth were recorded by TD every 6 seconds for fibrin formation and every 30s for thrombin generation during 60 min.

1D Data analysis

For the TD, an in-house code is developed in MATLAB R2021b in order to extract TD variables. Since the current dataset contains hypercoagulable plasma, spontaneous fibrin clots are being formed which can limit the field of view and therefore the measurements. The percentage of spontaneous clots in the field of view was automatically computed from the TD software. TD data is chosen to be discarded for further analysis once the spontaneous clots cover $> 40\%$ of the field of view.

The following parameters were obtained for the fibrin formation (see Fig. 3B): lag-time (Ft_{lag}, the time needed to see the beginning of clot growth), the initial rate of clot growth (Fv_i: slope of the clot size curve versus time calculated between 2 and 6 min. after clot growth start), stationary rate of clot growth (Fv_s: slope of the clot size curve versus time between 10 and 15 min after clot growth start), and clot size (*CS*: calculated at 15 min from the beginning of the clot growth). In addition, from TD more parameters can be calculated regarding the propagation of the thrombin peak (Fig. 3C)[40]. The first parameter is the amplitude of the thrombin peak (A_s), and the second is the rate of thrombin peak propagation (Tv_s). It is chosen to measure A_s at 10, 15 and 25 min, and to measure Tv_s at the time interval between 10 and 15 min.

The previously described TD fibrin and thrombin variables are also extracted from the 1D in silico data. To evaluate the predictive performance of the in silico model, the mean absolute percentage error (MAPE) and Lin's concordance correlation coefficient (CCC) are quantified. Lower MAPE values indicate better agreement, with a value of 0% representing perfect prediction. Lin's CCC values range from -1 to $+1$, with values above 0.90 typically considered indicative of strong agreement.

2D Methods

2D In silico model

The previously developed 1D model is further extended to a 2D scenario, in which is also solved for the flow by adding a convection term. The model consists of advection-diffusion-reaction equations, describing the spatio-temporal distributions of the factors described previously. For each factor, the following general equation now applies:

$$\frac{\partial X_i}{\partial t} + \nabla \cdot (\mathrm{u} X_i) - D_{X_i} \nabla^2 X_i = R \tag{2}$$

where $\frac{\partial X}{\partial t}$ represents the temporal change of the quantity X_i. The convection term is represented by $\nabla \cdot (\mathrm{u} X_i)$, which accounts for the transport of X_i due to the velocity field u. The diffusion term $D_{X_i} \nabla^2 X_i$ contains the protein-specific diffusion coefficient D_{X_i}. R is the reaction term, representing any generation or consumption of X_i, as was described in Table 2.

The fluid is modeled as an incompressible Newtonian fluid. The Navier-Stokes equation is used to describe the dynamics of blood flow in the vessel:

$$\rho \left(\frac{\partial \mathrm{u}}{\partial t} + (\mathrm{u} \cdot \nabla)\mathrm{u} \right) = -\nabla p + \mu \nabla^2 \mathrm{u} - \frac{\mu}{K_f} \mathrm{u} \tag{3}$$

$$\nabla \cdot \mathrm{u} = 0. \tag{4}$$

where u is the flow velocity, p is the pressure, ρ is the density of the blood, μ is the dynamic viscosity, and K_f is the hydraulic permeability of the fibrin clot which is based on the Davies' equation[33,55]:

$$\frac{1}{K_f} = \frac{16}{\alpha^2} \widetilde{F}_P^{\frac{3}{2}} \left(1 + 56 \widetilde{F}_P^3 \right)$$

where F_p is the ratio of fibrin polymer to fibrinogen, and α is the radius of the fibers which is set to 6×10^{-4} mm[33]. A threshold for the application of the hydraulic permeability of the clot is applied. This is based on the gelation point, which is estimated to occur when about 15% to 20% of the fibrinogen has been incorporated into the gel[56,57]. In all simulations the initial fibrinogen concentration is set to an average value of 7000 nM (Table 4); therefore, the fibrin polymer threshold for the application of the Davies' equation is set to 15% of 7000 nM, which is 1050 nM.

The viscosity and density in this model are adopted from Taylor et al.[58], and are defined as 3 cP and 1060 $\frac{kg}{m^3}$, respectively. As coagulation model parameter input, three patient-specific parameter sets are implemented in the 2D scenario. These three cases are based on the earlier obtaind TG curves, where the case with lowest, highest, and medium peak height p_h are chosen. From now on, these will be refered to as the hypo- (P_{hypo}), hyper- (P_{hyper}), and normal (P_{normal}) coagulation case, respectively.

The simulations are solved with a fully-coupled implicit manner using the Finite Volume Method, using ANSYS Fluent (ANSYS Inc., Canonsburg, PA, USA; version 2024 R1; https://www.ansys.com/). For the simulations, four types of geometries are considered: (1) a 2D rectangular geometry, based on the in vitro experiments performed by Shen et al.[19], (2) a 2D Backward Facing Step (BFS) geometry, based on the in silico and in vitro experiments performed by Taylor et al.[58], (3) a 2D one-sided stenosed geometry, and (4) 3D patient-specific geometries (see Fig. 4). These geometries are explained in more detail in the next sections.

2D flow model validation

At first, in order to compare the flow simulations with in vitro data, the setup of the experimental study performed by Shen et al. (2008) is recreated (Fig. 4A). The domain consists out of a 0.45x10mm long 2D channel, with a TF patch of 0.2mm placed at 2mm from the inlet. As proposed by Shen et al. (2008), varying shear rates and TF patch sizes are applied to investigate its effect on the initiation time of the fibrin clot. A steady parabolic inlet velocity profile was imposed, with wall shear rates varying from $5s^{-1}$ to $40s^{-1}$. Flow was allowed to reach a steady-state solution before activation of the coagulation model. A constant outlet pressure of zero was specified, and no-slip boundary conditions were applied at all domain walls. TF patch sizes are varied from 0.1 mm to 1.6 mm. In the in silico simulation, the clot initation time is measured at the most distal side of the TF patch, and quantified as the time it takes for the fibrin polymer to reach a value of 1050 nM, which is assumed to be the

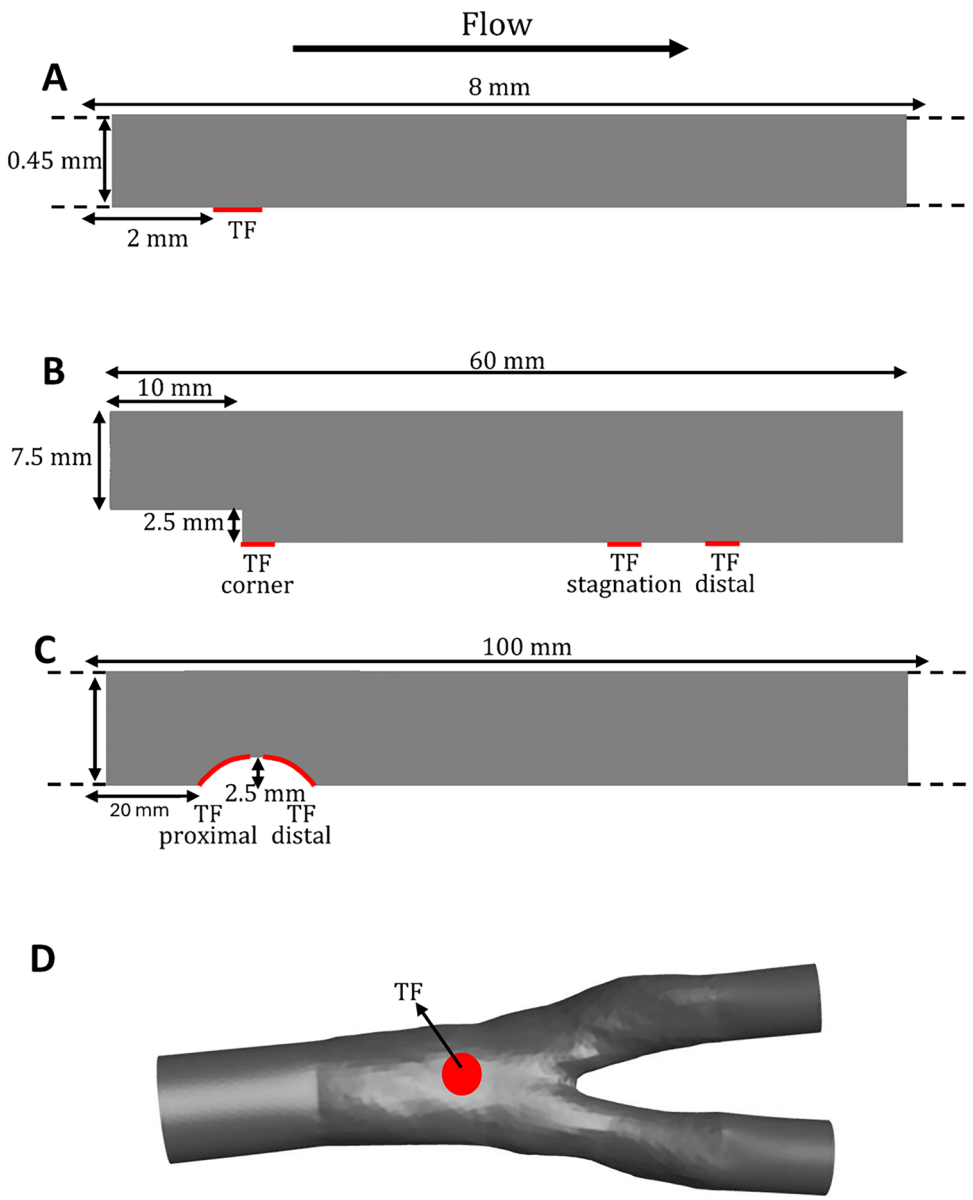

Fig. 4. Geometries of the 2D and 3D computational domains, with indicated tissue factor (TF) patches in red. (**A**) Rectangular geometry, (**B**) original backward-facing step (BFS), (**C**) stenosed geometry with 25% stenosis, and (**D**) a 3D patient-specific geometry. In all configurations, flow is applied at the left boundary.

gelation concentration, as explained in the previous section. A 2D uniform mesh is generated with an isotropic element size of 10 μm, and a timestep of 0.01s is applied. The flow is simulated for 20min. The patient-specific parameter set P_{normal} is used in this model.

2D Backward-facing step

The BFS geometry was employed as a benchmark to investigate the effects of varying flow conditions on the formation and growth of fibrin clots. The BFS geometry proposed by Taylor et al.[58] was reconstructed with dimensions of 10×60 mm and a step height of 2.5 mm (Fig. 4B). As the mesh and temporal sensitivity analyses were previously conducted by Taylor et al.[58], the spatial and temporal resolutions were adopted. This resulted in an isotropic cell size of 139 μm and a time step of 10 ms. In order to match the setup of Taylor et al. and to be able to compare outputs, their steady parabolic inlet velocity profile was applied at the inlet, with a mean velocity of 0.23 m/s (Re = 490)[58], resulting in an initial wall shear rate of 183 s^{-1}. The remaining flow conditions are similar as in the previous 2D flow model simulation. Additionally, a case with a lower initial wall shear rate of 100 s^{-1} was examined. Furthermore, a BFS geometry with a gradual step is created in order to investigate the effect of step steepness, of which the dimensions and settings are copied from the original BFS geometry. In order to investigate the effect of injury location with respect to the recirculation zone, a TF patch of 2.5 mm in size was placed at three distinct locations: 1) at the step corner ("TF corner"), 2) at the center of the stagnation point ("TF stagnation"), and 3) 2 mm downstream from the stagnation point (beyond the recirculation zone, "TF distal"). The patient-specific parameter values for the normal coagulation plasma (P_{normal}) was incorporated into the model. The flow was simulated for two hours. The fibrin clot dimensions over time, in terms of area and height, were analyzed using ANSYS CFD-Post (ANSYS Inc., Canonsburg, PA, USA; version 2024 R1; https://www.ansys.com/), for which the clot area was taken as the region where the fibrin polymer exceeded the 1050 nM threshold.

2D Stenosed geometry

The stenosed geometry was employed to investigate the effects of mild stenosis on patient-specific fibrin formation in a 2D rectangular blood vessel (Fig. 4C). The overall channel height and the stenosis height were set equal to those of the BFS geometry, measuring 10 mm and 2.5 mm, respectively. The stenosis severity is set to 25%, which falls within the stenosis range observed in the PARISK study[50]. The computational mesh consisted of quadrilateral cells with a primary grid resolution of 139 μm, as is used in the BFS scenario. The three selected patient-specific parameter variations (P_{hypo}, P_{hyper}, and P_{normal}) were incorporated into the model. Again, blood flow was driven by a parabolic velocity profile at the inlet and a pressure outlet, with a mean inlet velocity of 0.23 m/s. No-slip boundary conditions were imposed at all domain walls, and the outlet pressure was set to zero. The TF patch, measuring 2.5 mm in length, was positioned at two locations: on the upstream of the stenosis, and downstream side of the stenosis. Flow was simulated for a total duration of two hours, after which the fibrin clot area over time was analyzed.

3D Methods

3D In silico model

For the patient-specific analysis, MRI-based geometries of the symptomatic carotid arteries were obtained from a selection of patients enrolled in the PARISK study. Patients who underwent contrast-enhanced computed tomography angiography (CTA) and MRI of their carotid arteries at baseline and after two years of follow-up were included in the study. A pre-selection was made of two patients who demonstrated an ulcer at follow-up, of which one already had an existing ulcer at baseline. The lumen geometry was previously generated by Dilba et al., who created the 3D geometry of the carotid bifurcation using MRI contours. Subsequently, in the current study, a triangular surface mesh and hexahedral-core mesh with three boundary layers, a minimum and maximum element size of 140 and 280 μm, respectively, and a growth rate of 1.2 was generated using ANSYS Fluent Meshing (ANSYS Inc., Canonsburg, PA, USA; version 2024 R1; https://www.ansys.com/), resulting in 393023 and 428966 elements for patient A and B, respectively. The arterial wall was assumed to be rigid, and a no-slip boundary condition was applied at the wall. At the inlet of the common carotid artery (CCA), a parabolic velocity profile was prescribed, based on the average flow curve. The flow division between the internal carotid artery (ICA) and external carotid artery (ECA) was assumed to follow typical physiological proportions, with 64% of the flow directed towards the ICA and 36% towards the ECA[59]. The blood is modeled with the same conditions as previously described. The TF patch was projected at the location where the follow-up ulcer was identified. For further details on the model setup and ulcer determination, refer to Dilba et al.[59]. Blood flow was simulated for a duration of 15 min.

Results

0D - In vitro and in silico curve fitting

At Erasmus Medical Center, plasma of 54 patients enrolled in the PARISK study was available, with which the TG assay was previously conducted and the 0D in silico model was fitted against the resulting 0D in vitro TG curves. The curve-fitting procedure was effective for all 54 patients, including both high and low TG profiles, as demonstrated by three selected, representative cases (P_{hypo}, P_{hyper}, P_{normal}) in Fig. 5A. The resulting parameter values obtained from curve fitting of all patients are summarized in Fig. 5B. Parameter values for the three representative samples are given in Supplementary Table S2. Note that additional reaction rates $k10$ and $k13$ are presented, which originate from the scaling process as part of the curve fitting procedure (see Supplementary Information S2).

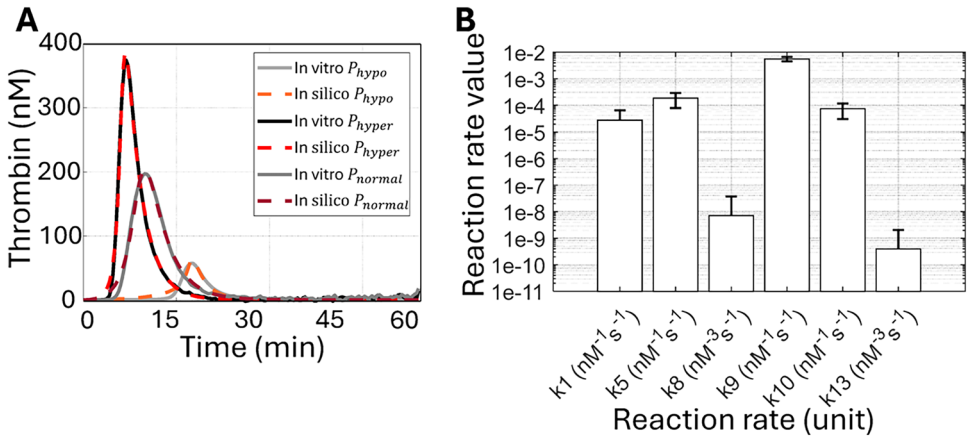

Fig. 5. Results of 0D in silico curve fitting of thrombin generation (TG) in vitro data. (**A**) In silico (dashed lines) vs in vitro (solid lines) comparison of the thrombin generation curve for three representative plasma samples (P_{hypo}, P_{hyper}, P_{normal}). (**B**) Patient-specific parameter values for all available plasma samples (N=54), presented as mean with standard deviation, visualized at log-scale.

1D - In silico and in vitro

The 20 pre-selected samples were used for further TD analysis, of which three were excluded due to the formation of spontaneous clots within 10 min, which obstructed the field of view and prevented the extraction of variables for analysis, and one sample was excluded due to a saving error of the system. Consequently, 16 samples were analyzed in total, with both TG and TD assays performed.

The results of the in silico model and in vitro TD for the three representative samples (P_{normal}, P_{hypo}, P_{hyper}) are presented in Fig. 6. Figure 6A depicts the population's normal coagulation case (P_{normal}). In the in vitro results, the thrombin peak decreases and stabilizes at approximately 100 nM after 30 min. The in silico model also predicts a similar stabilized thrombin concentration, although stabilization occurs earlier, at approximately 15 min. The thrombin wave propagation shows good agreement, with the thrombin wavefront in both in silico and in vitro systems reaching about 2.3 mm at 55 min. The fibrin clot growth dynamics in this case also align well. Both in vitro and in silico exhibit a short lag-time, followed by an initial exponential growth and a linear increase in fibrin clot size.

Figure 6B demonstrates a hypo-coagulable case (P_{hypo}). The in silico and in vitro thrombin peak profiles are closely matched, with both showing a relatively slow decay that stabilizes at around 25 nM after 40 min. The thrombin wave speed also aligns, with both methods showing about 1.1 mm propagation after 55 min. The fibrin clot growth curves also exhibit reasonable agreement, characterized by an initial exponential growth followed by a linear increase after 20 min. However, a discrepancy is observed in the lag time predicted by the in silico model, which appears to be underestimated compared to the in vitro result.

Figure 6C shows the findings for P_{hyper}, representative of a hyper-coagulable state. In the in vitro system, the thrombin concentration peaks initially at approximately 400 nM and keeps increasing over time. The in silico thrombin amplitude is consistently lower compared to the in vitro case, and in contrast does not increase over time. Alhtough the thrombin amplitudes thus do not seem to match well, the fibrin clot growth speed does seem to align between in vitro and in silico, with both showing a quick linear increase over time. It must be noted that in this case, spontaneous clots formed quickly around 22 min, after which further tracking of thrombin and fibrin was not possible.

Figure 7 presents a comparison of the spatio-temporal fibrin and thrombin variables between the in silico simulations and in vitro observations for all included samples (N=16). The results indicate strong agreement between the model and experimental data for clot size at 15 min (Fig. 7B), as well as for the initial and stationary slopes (Fig. 7C and D, respectively), with MAPE values of 4.6, 4.5, and 8.0% and CCC values of 0.96, 0.95, and 0.96, respectively. However, as previously observed in Fig. 6, the in silico lag time is underestimated relative to the in vitro observations, leading to a higher MAPE of 41.5% and a CCC of 0.63 (Fig. 7A). Good agreement is observed for the thrombin wave speed (Fig. 7H), with an MAPE of 8% and a CCC of 0.95. Although the CCCs for the thrombin amplitude is high at all timepoints (> 0.85), the in silico model seems to consistently underestimate the thrombin amplitude, leading to a maximum MAPE of 28.3% (Fig. 7E–G). Note that clusters corresponding to the original sample pre-selection are visible for most variables, with the exception of fibrin lag time. Samples selected from the lower inter-quartile range of TG ETP and/or peak height (grey scatter dots) consistently show reduced values across variables, whereas those from the upper inter-quartile range (black scatter dots) exhibit higher values.

2D - In silico

Validation

Figure 8 shows the results of the initial validation step of the flow simulations, including a 2D rectangular geometry, with applied varying wall shear rates and TF patch sizes. The results are compared with the in vitro experiments performed by Shen et al.[19]. The parameters used in the in silico model are taken from the normal-

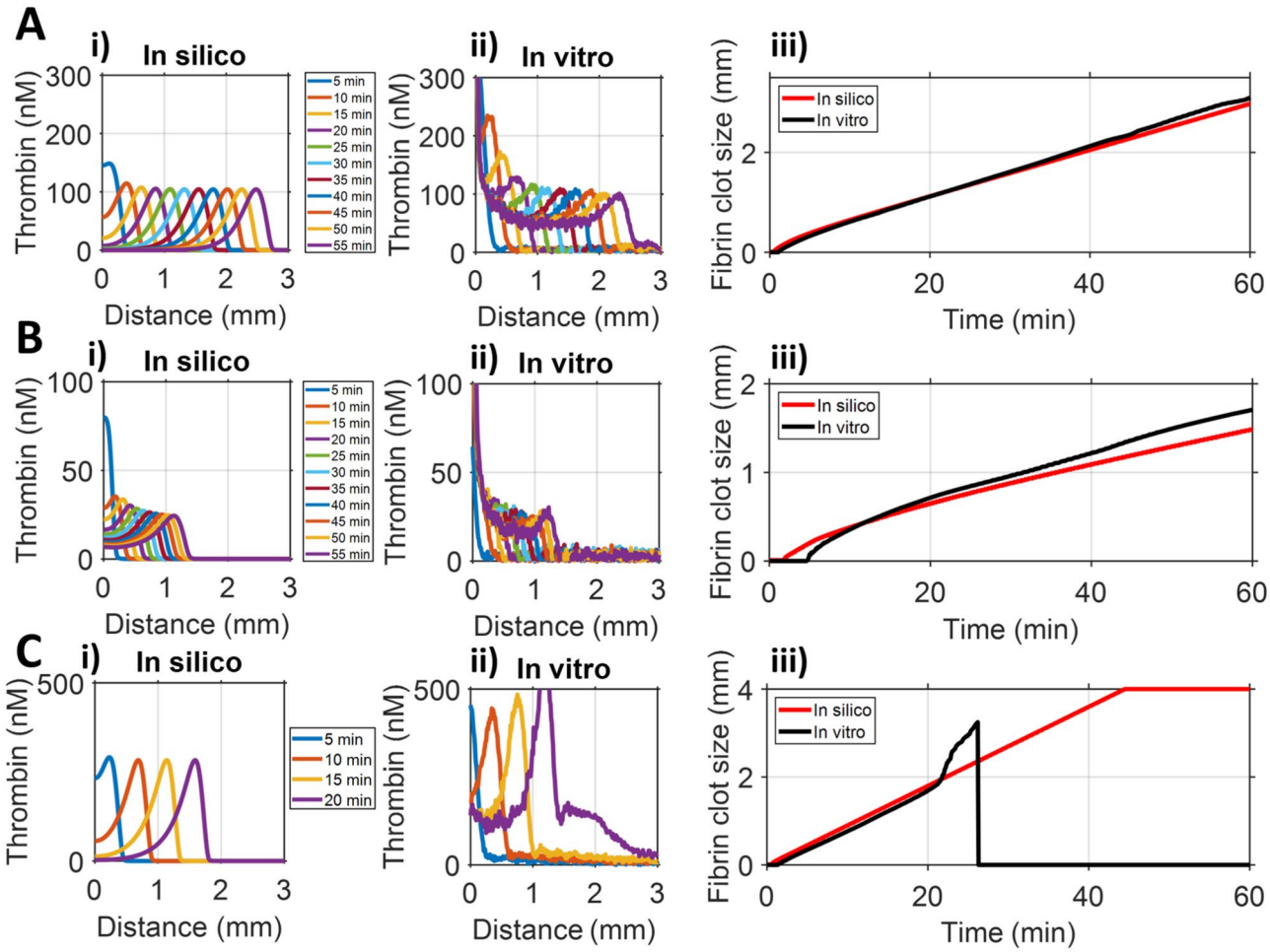

Fig. 6. In silico vs in vitro comparison of fibrin clot growth parameters, for (**A**) P_{normal}, (**B**) P_{hypo}, and (**C**) P_{hyper}. The left- and middle subfigures represent the thrombin profiles at 5-minute intervals, in silico (i) and in vitro (ii) respectively, with each colour representing a different timepoint. The right subfigures (iii) show the in silico and in vitro superimposed fibrin clot growth curves. For each sample, the y-axis range is adjusted.

coagulation plasma type. Figure 8A and B show the fibrin profiles at a shear rate of $40s^{-1}$ and $5s^{-1}$, for the in vitro and in silico model, respectively. It can be seen that for both cases, at a shear rate of $40s^{-1}$ no fibrin is being formed at 30 and 300 seconds. However, in both cases, when a shear rate of $5s^{-1}$ is applied, fibrin is formed at 300 seconds. Also a similar pattern can be observed: a steep increasing peak above the TF patch, and a gradually decreasing fibrin tail behind the TF patch, caused by the flow. The in silico model however predicts a sharper peak compared to the in vitro model.

Figure 8C shows the clot initiation time, measured at varying shear rates. It can be observed that a shear rate threshold of approximately 25 s^{-1} can be quantified for both the in vitro and in silico case. However, the in silico model shows a gradual increase in clot initiation time, until the quantified shear rate threshold of 25 s^{-1} is reached, whereas in the in vitro case the clot initiation time remains low ($< 200s$) until the quantified shear rate threshold is reached.

Figure 8D shows the observed clot time for varying patch sizes (at a fixed shear rate of 40 s^{-1}). Here, it can be observed that for the in silico model a patch size threshold of 800 μm is required to observe clot formation below 800 seconds. Nevertheless, a patch size of 400 μm in the in silico model showed clot formation just right after 800s. This matches well with the in vitro situation, where in two out of three experiments at a 400 μm TF patch the clot was initiated within 800s, whereas at the third experiment at a 400 μm TF patch the clot was not formed within 800s.

Backward facing step

Figure 9 shows the BFS simulation results, examining how TF patch location (corner, stagnation point, and distal from the recirculation zone) and wall shear rates (original: 183 s^{-1} vs. low: 100 s^{-1}) affect fibrin clot growth. In the TF-corner scenario, Fig. 9A shows that the clot is notably larger after 2 hours at the lower shear rate (ii), compared to the original shear rate (i). Although growth in area and average height is similar during the first 15 min, the low-shear case accelerates more quickly thereafter, especially in overall area (Fig. 9Aiii). Figure 9Aiv shows that in the TF-corner case the clot increases in average height until it reaches the maximum height of the

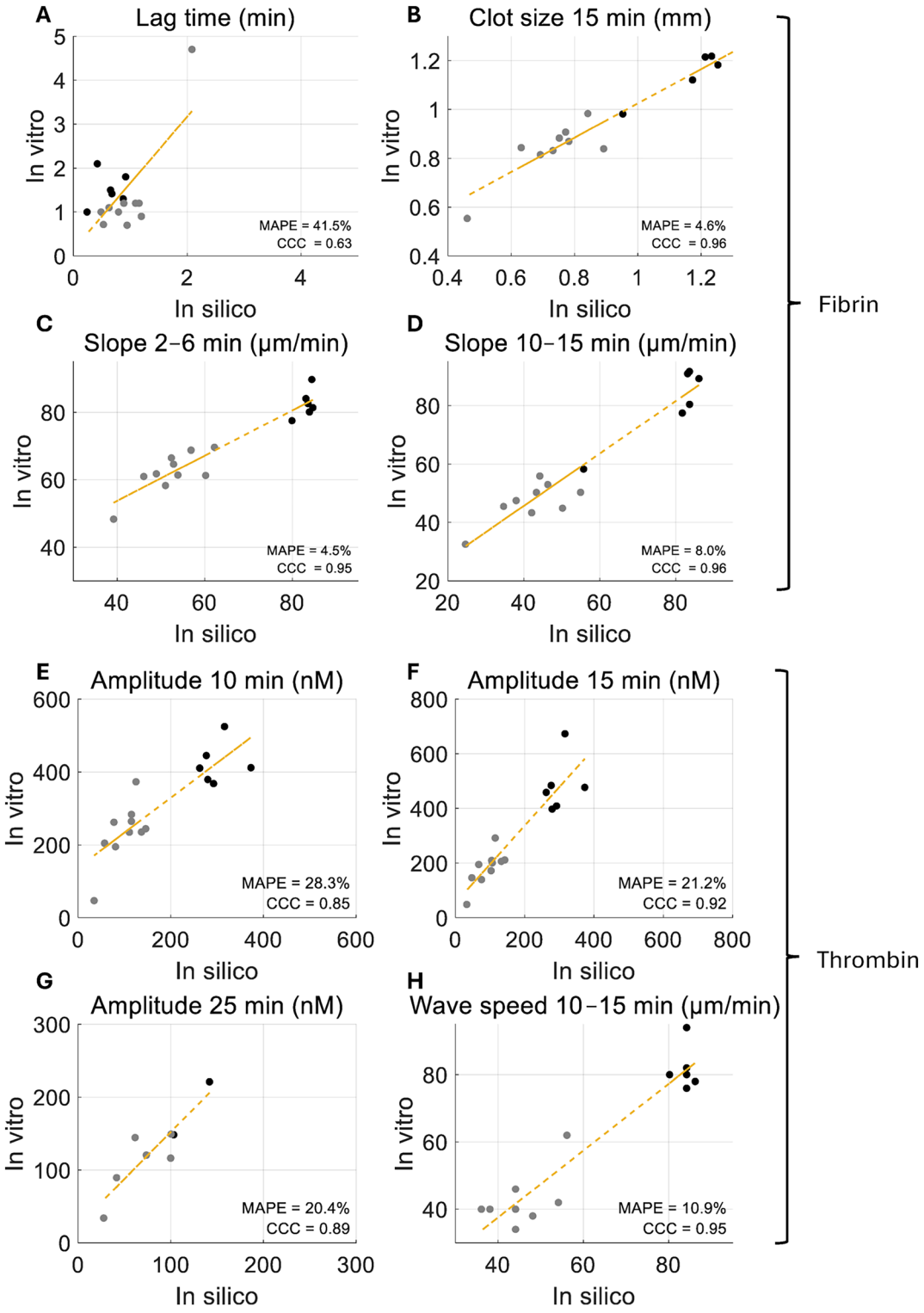

Fig. 7. In silico vs in vitro comparison of fibrin clot growth and thrombin parameters. The correlation of (**A**) fibrin lag time, (**B**) fibrin clot size at 15 min, (**C** and **D**) fibrin front propagation slopes during early (2–6 min) and late (10–15 min) time windows, respectively. Correlation of thrombin amplitude at (**E**) 10 min, (**F**) 15 min, and (**G**) 25 min. (**H**) Correlation of thrombin wave speed between 10–15 min. Each panel includes the mean absolute percentage error (MAPE) and Lin's concordance correlation coefficient (CCC) as measures of model agreement. Grey and black dots represent the pre-selected samples within the lower- and upper inter-quartile range of all available samples, respectively, of the original thrombin generation area-under-the-curve (ETP) and/or thrombin generation peak height.

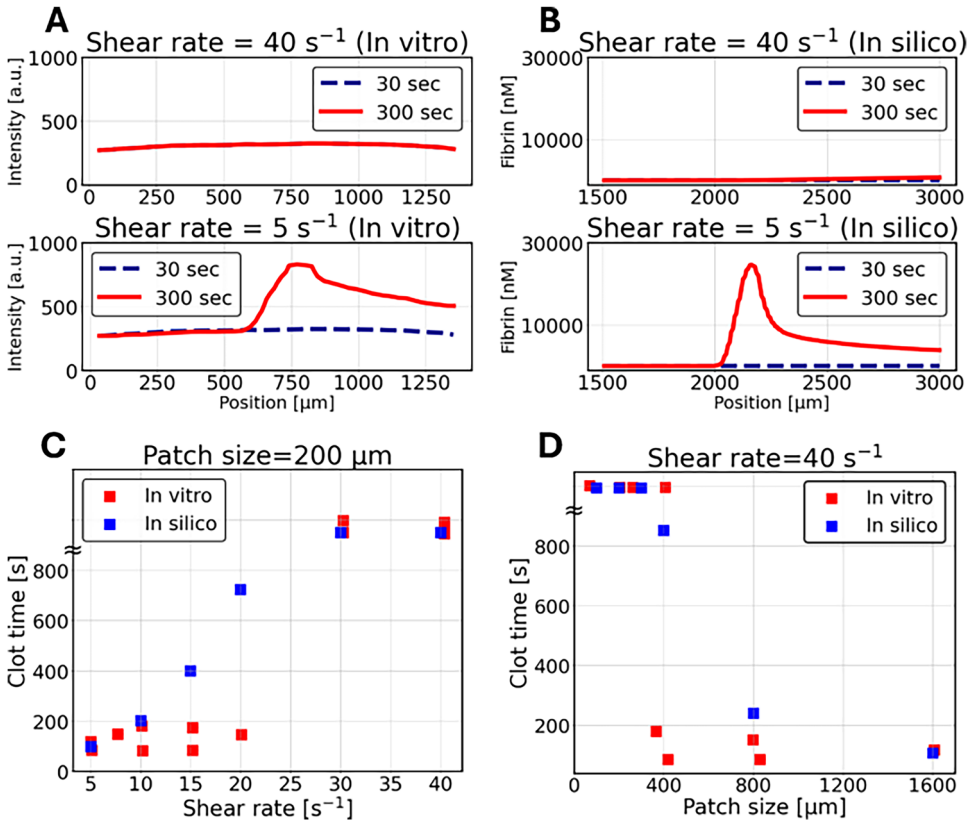

Fig. 8. Comparison of in vitro and in silico fibrin accumulation under flow. (**A**) Fibrin intensity profiles measured in vitro at shear rates of 40 s^{-1} (top) and 5 s^{-1} (bottom), showing spatial distributions at 30 s (blue dashed) and 300 s (red solid). In vitro data adopted from Shen et al.[19]. (**B**) Corresponding fibrin concentration profiles from the current in silico model under the same shear conditions. (**C**) Clot initiation time versus shear rate for a fixed patch size of 200 μm, comparing experimental (red squares) and simulated (blue squares) results. (**D**) Clot initiation time versus patch size at a fixed shear rate of 40 s^{-1}.

step, and touches the high-velocity region above the step. Subsequently, the clot grows more in its length, but not in its height and slowly fills up the recirculation zone. It was observed that the thrombin profile travels as a wave, as was observed in the 1D in vitro and in silico models (see Supplementary Fig. S5A). Therefore, thrombin is for the majority only present at the fibrin high-concentration front, and not in the core of the fibrin.

Figure 9B shows the results when the TF patch lies in the middle of the stagnation point. Then, the clot develops both upstream and downstream, with the downstream portion becoming taller and covering a greater area. The flow separation and the recirculation zone, in combination with the step, seem to cause accumulation of coagulation factors on the upstream side. At lower shear, again, the overall area and height increase more rapidly. When the TF patch is placed distally from the stagnation point, only a thin, minor fibrin layer is formed (see Supplementary Fig. S5C).

When comparing the three TF patch locations, the largest clot is formed when the TF patch is placed in the stagnation zone (maximum area of 82mm^2), forming in both upstream and downstream directions, compared to the TF patch in the corner and at the distal location (maximum area of 24mm^2 and 7mm^2, respectively). Across all TF locations, a lower shear rate consistently accelerates clot growth. Furthermore, it was observed that thrombus growth in a gradual BFS is less extensive than in the steep BFS (see Supplementary Fig. S6).

Stenosis

Continuing to the stenosed geometry, Fig. 10 illustrates clot growth after one hour (left) and two hours (right) when the TF patch is positioned either on the proximal (Fig. 10A,B) or distal (Fig. 10C,D) side of the stenosis. In both the proximal and distal case the hypo-coagulation plasma shows negligible clot formation over the whole timespan. In contrast, the hyper- and normal-coagulation plasma types grow at a similar pace initially, but the hyper-coagulation clot displays substantially faster growth after roughly 30 min in the proximal case (Fig. 10B), and after 60 min in the distal case (Fig. 10D). Considering the TF patch location, at two hours the fibrin covered area is 0.41 mm^2, 0.16 mm^2 , and 0.01 mm^2 for the hyper-, normal, and hypo-coagulation at the proximal side, respectively, vs. 4.6 mm^2, 2.1 mm^2, and 0.05 mm^2, for the hyper-, normal, and hypo-coagulation at the distal side, respectively. Thus in general, for all plasma types the clot covers a larger area when the TF patch is placed distally, compared to when the TF patch is placed proximally.

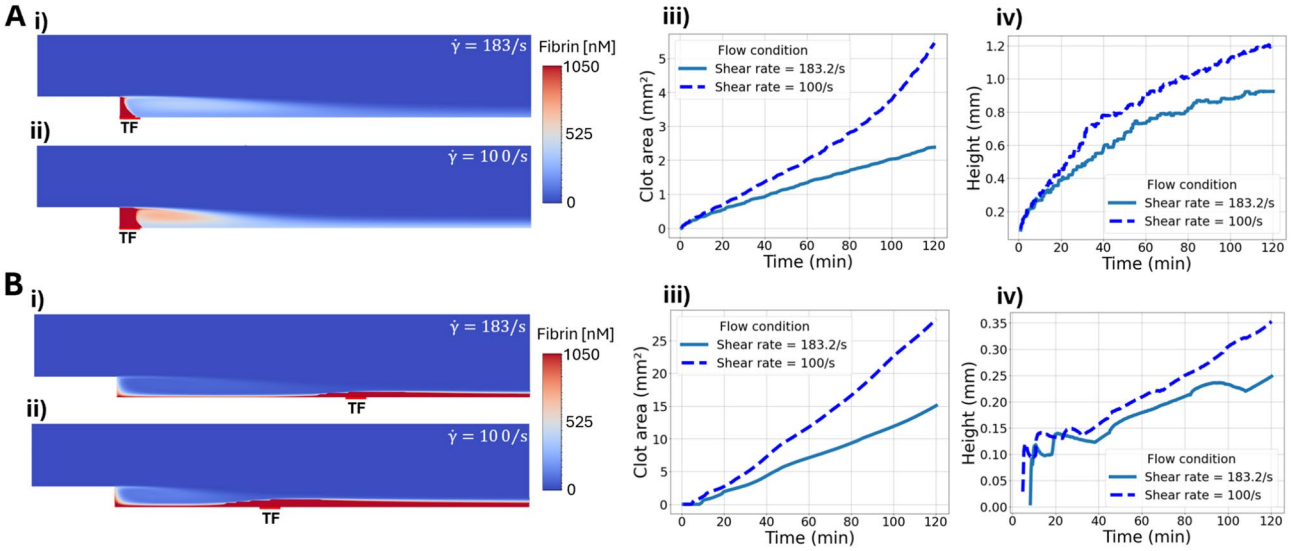

Fig. 9. Backward facing step: simulated fibrin clot growth metrics under different shear rates and tissue factor (TF) locations. (**A**) Fibrin (i-ii) concentration profiles at 120 min under high (183 s^{-1}, top) and low (100 s^{-1}, bottom) shear rates, with TF located at the step corner. iii-iv) Clot area growth and average height, respectively, over time corresponding to conditions in (A), for both shear rates. (**B**) Fibrin (i-ii) profiles under high and low shear conditions, with TF positioned in the stagnation point. iii-iv) Clot area growth and average height, respectively, over time corresponding to conditions in (**B**), for both shear rates. In all plots, blue solid lines represent high shear (183 s^{-1}), and blue dashed lines represent low shear (100 s^{-1}). Color maps indicate concentrations of fibrin (0–1050 nM).

3D - In silico

Figure 11 presents the results of the 3D simulations of fibrin clot formation in two patient-specific carotid artery geometries. Although fibrin concentrations in both cases remain below the gelation threshold (< 1050 nM), the simulations show a clear difference in thrombotic potential between the patients. In Patient A (Fig. 11A), a pronounced stenosis in the internal carotid artery produces a peak wall shear rate of approximately 4000 s^{-1}. Upstream and downstream of the stenosis, however, regions of reduced shear are evident (see zoomed-in wall shear rate on the right). The TF patch, represented by factor Xa, is located within one of these low-shear zones ($\approx$150 s^{-1}), where fibrin polymer accumulation is clearly observed. In Patient B (Fig. 11B), no severe stenosis is present, and the wall shear rate near the TF patch, again represented by factor Xa, is higher ($\approx$400 s^{-1}). The fibrin polymer concentration in Patient B is lower than in Patient A, and appears to be elongated along the flow direction, suggesting washout by the bloodstream. Furthermore, the maximum concentration of factor Xa in Patient B is 1 nM lower than in Patient A, reflecting a minor difference in coagulation initiation between the two patients.

Discussion

This study introduces a unified workflow that calibrates a reduced coagulation model on TG data, validates it with TD within the same cohort, and subsequently propagates the same patient-specific parameters without additional tuning into multi-dimensional flow simulations and patient-specific vascular geometries. The fitted 0D model showed good agreement with the in vitro TG data. The 1D model reproduced experimental observations with strong quantitative agreement for clot size (MAPE = 4.6%) and for both the initial and stationary clot growth rates (MAPE = 4.5% and 8.0%). Good correspondence was also achieved for thrombin wave speed (MAPE = 8%), and although the in silico model tended to underestimate thrombin amplitude (maximum MAPE = 28.3%), the overall correlation remained strong (CCC > 0.85). Furthermore, 2D simulations revealed that a minimum TF patch size and an upper shear rate limit are required for fibrin formation, confirming in vitro results from other studies[19]. Notably, the 2D in silico model reproduced the in vitro outcomes without any additional parameter adjustments beyond the initial 1D calibration. Beyond reproducing these outcomes, the framework provided novel mechanistic insights under hemodynamic conditions. First, the location of the TF region relative to recirculation zones strongly influenced fibrin clot growth. Second, in stenosed geometries, distal clots consistently outgrew proximal clots across all plasma types. Third, 3D simulations in patient-specific carotid models demonstrated the combined effect of flow, geometry, and plasma composition on fibrin formation. In contrast to previous approaches[28,38], our model employs a reduced number of variables and parameters, thereby improving computational efficiency while retaining predictive accuracy. By integrating patient-specific parameterization, experimental validation, and flow-resolved simulations within a single framework, this work carefully bridges standard coagulation assays with vascular hemodynamics.

In this study, we initiated our workflow with a curve-fitting strategy to tune the parameters of the the 0D coagulation model to in vitro TG data from all 54 patients. While this approach accurately reproduced measured

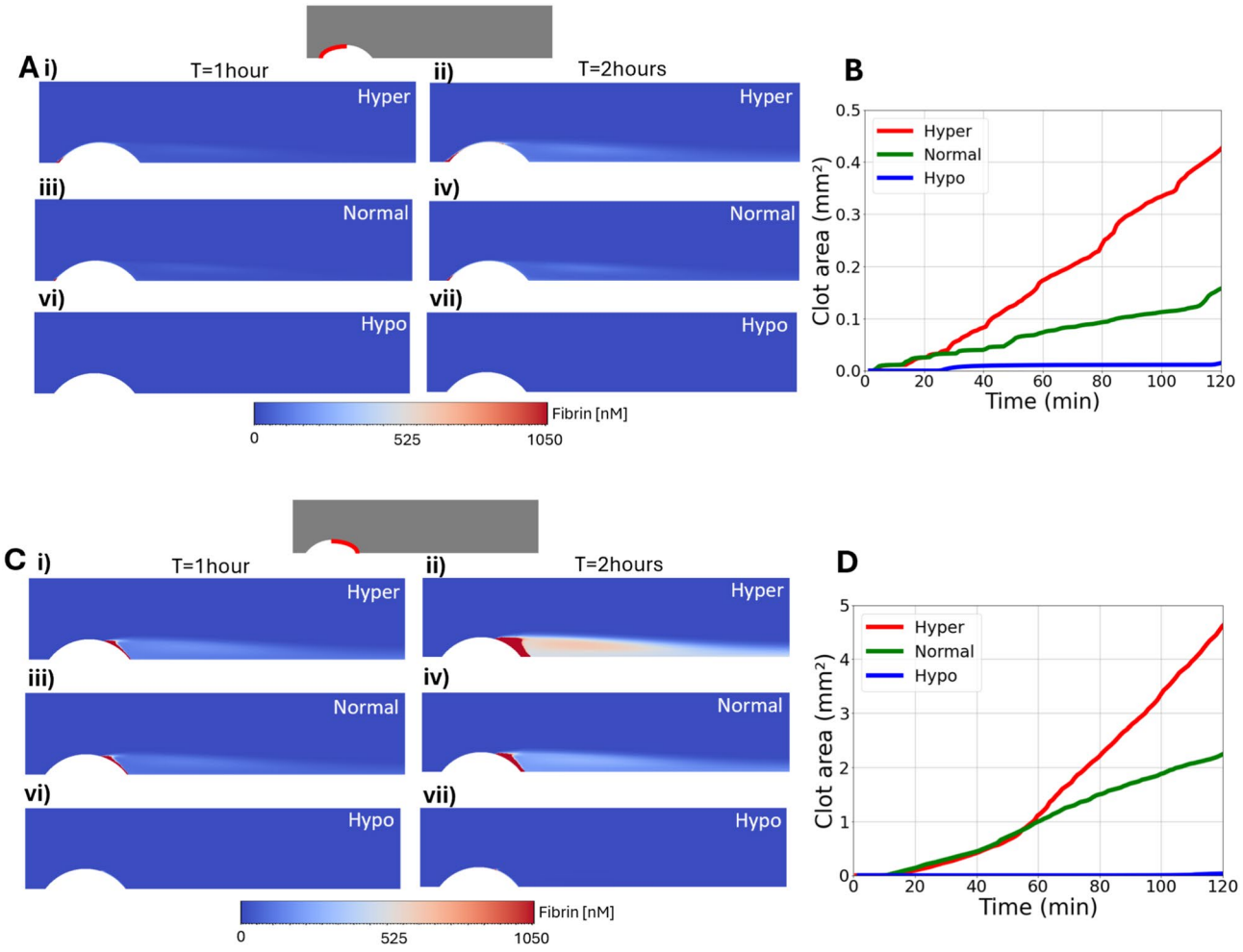

Fig. 10. Simulated fibrin clot growth in a stenosed geometry. (**A**) Fibrin concentration at TF patch location at the proximal side of the stenosis, visualized at 1 hour (left column) and 2 hours (right column) for hypercoagulable (i–ii), normal (iii–iv), and hypocoagulable (vi–vii) plasma types. The fibrin concentration is visualized using a color scale ranging from 0 to 1050 nM. (**B**) Quantification of clot area over time in the proximal region for hypercoagulable (blue), normal (orange), and hypocoagulable (green) cases. (**C**) Fibrin concentration at TF patch location at the distal side of the stenosis at 1 hour (left column) and 2 hours (right column), again shown for hypercoagulable (i–ii), normal (iii–iv), and hypocoagulable (vi–vii) plasma conditions. (**D**) Clot area growth over time in the distal region for the three plasma types, using the same color scheme as in (**B**).

TG curves, concerns have been raised about the reliability of kinetic modeling for thrombin generation[25,42]. A key issue is the large variability in reported parameter values in literature: for instance, K_m for prothrombin conversion spans three orders of magnitude (K_m = 8.6–1060)[42], and the rate of factor XI activation varies up to five orders of magnitude[35]. Consequently, this variability introduces considerable uncertainty when making use of literature-derived parameters in predictive models[42]. To address this, we applied data-driven parameter identification, as done in prior studies. For example, Mendez et al. (2019) also fitted their contact-activation model due to the non-physiological conditions under which many kinetic parameters were originally determined[24,60]. In the current model, a linearized, parameter-calibrated form of the thrombin–fibrinogen kinetics was employed, prioritizing computational efficiency and accurate reproduction of TD observations rather than strict adherence to Michaelis–Menten kinetics. Although the current model showed good agreement with in vitro data, a more mechanistic non-linear formulation could be explored in future work.

The 1D in silico model showed good agreement with in vitro measurements for thrombin wave speed, fibrin clot size, and fibrin growth rates, demonstrating its ability to reproduce key experimental trends. The model also captured the significant differences observed between patient plasma samples, suggesting that it can represent patient-specific variations in fibrin formation. Furthermore, the TD assay proved to be a valuable tool for generating patient-specific spatio-temporal fibrin data that can be readily integrated into in silico frameworks. While these results are encouraging, some discrepancies were observed, particularly in thrombin amplitude and fibrin lag time. These deviations may arise from model simplifications, such as the simplified fibrin polymerization[61], neglecting fibrin microstructure, and the dependence of clot permeability on thrombin

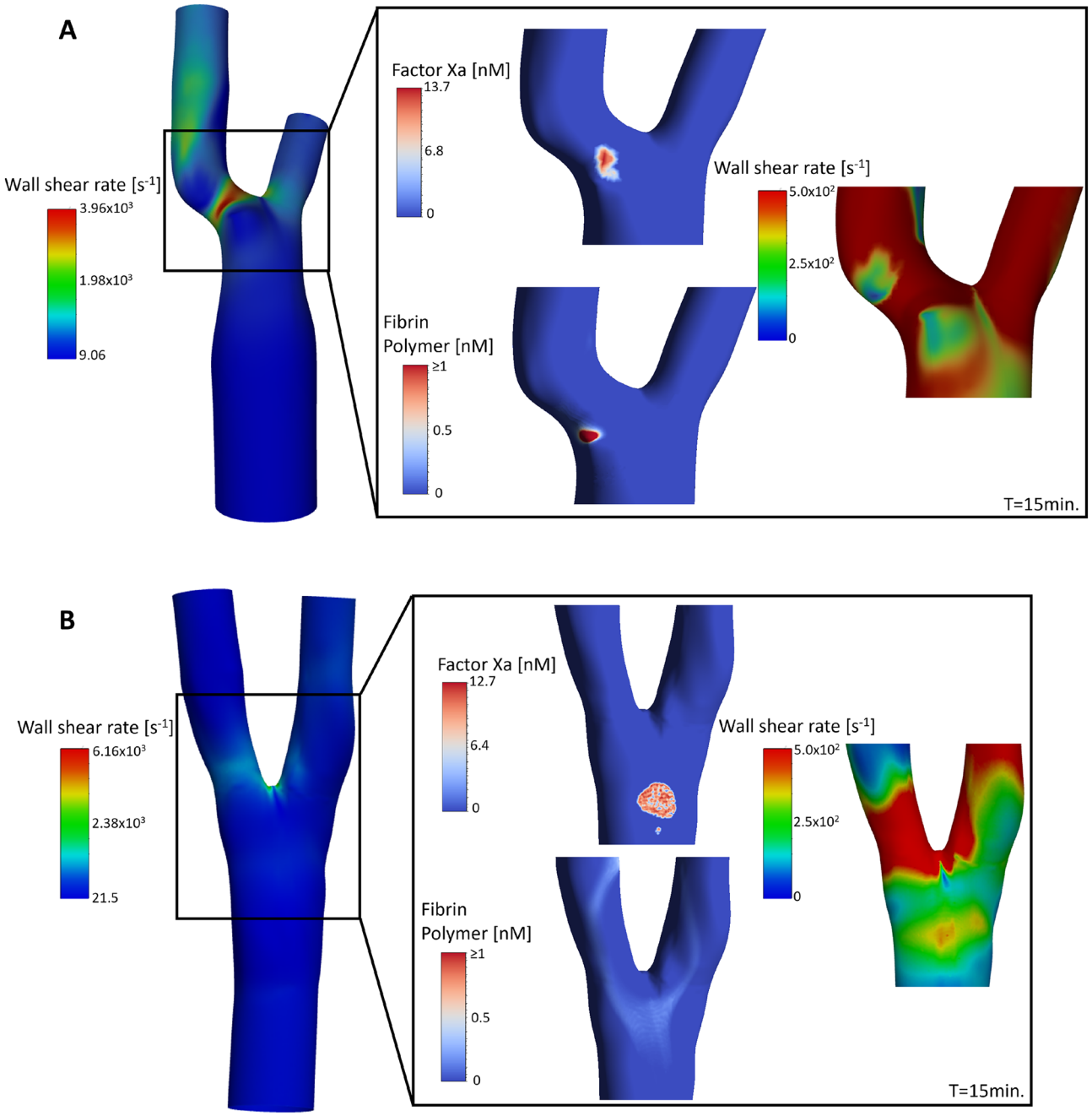

Fig. 11. 3D simulations of fibrin clot formation in two patient-specific carotid artery geometries (Patient A and B). Left panels show the full vascular geometries with wall shear rate distributions. Right panels provide zoomed-in views, displaying wall bound-concentrations after 15 min. of simulated physical time of factor Xa (serving as a proxy for the tissue factor patch, visualized on a global concentration scale), fibrin polymer (visualized on a 0–1 nM scale for clarity), and wall shear rate (visualized on an adjusted range of 0-500 s^{-1}). The true maximum fibrin polymer concentrations are 5.57 nM for Patient A and 0.36 nM for Patient B. Flow direction is from bottom to top.

and fibrinogen[14,62,63]. In reality, elevated thrombin concentrations produce denser fibrin networks with thinner fibers and smaller pores, which reduce the permeability[62,64], and higher fibrinogen concentrations further reduce the clot's permeability[14,63]. These structural changes modulate thrombin transport and retention within the forming clot, thereby potentially altering both the thrombin amplitude and the timing of fibrin formation observed experimentally[14,64]. Furthermore, challenges such as variability in plasma handling and spontaneous clot formation remain areas that require further investigations[40,41].

Other, more extensive, 1D computational models of TF-induced coagulation have been developed previously. Pisaryuk et al. [38] estimated patient-specific coagulation profiles from routine assays using a 78-variable model, by

adjusting initial coagulation factor concentrations, which were assumed to be proportional to assay outcomes. Although their model reproduced thrombin and fibrin dynamics in normal pooled plasma, it failed to capture clot growth in patient plasma. Kuprash et al.[28] developed a 37-variable model and explored the influence of coagulation factor deficiencies, by adjusting factor concentrations based on participant data. While they reported qualitative agreement with TD experiments, they did not provide quantitative validation, and their results showed notable differences in thrombin propagation. In contrast, our model includes only 6 variables and quantitatively reproduces key aspects of in vitro clot formation, achieving a balance between model complexity and predictive accuracy, making it more applicable in advanced CFD simulations. Our model focuses on identifying and calibrating the most sensitive kinetic rates, supported by sensitivity analysis, an aspect not incorporated in the previously discussed, more extensive coagulation models. The strength of our approach lies in consistently fitting this reduced set of key kinetic rates to the full patient-specific TG time course, rather than adjusting initial factor concentrations. Our findings may also indicate that TG dynamics are closely correlated with TD outcomes, suggesting that TG may serve as an effective predictor of fibrin formation at larger scales.

Subsequently to the 1D model validation, we applied the model in a 2D domain with the addition of flow. The in silico model showed a comparable shear rate threshold and TF patch size threshold, and thus seems to match well with in vitro experiments[19]. Importantly, our 2D model did not require any additional parameter calibration beyond the 1D model. This is in contrast to other studies, which required further tuning of model parameters using flow-specific experimental data[33,60]. Nevertheless, some studies have aimed to validate their coagulation-under-flow model in a similar manner, without parameter calibration based on prior flow experiments. For instance, Biscombe et al. implemented and adjusted two models previously developed by Jordan et al. and Dydek et al.[31,34,65], and compared their model with experiments of thrombin generation under diffusion[66] and under flow[19]. While some models yielded encouraging results, none robustly captured the behavior observed in both 1D diffusion and 2D flow experiments.

Our BFS simulations yielded three key findings. First, lower shear rates led to increased clot growth, consistent with model validation and prior experimental data[19]. Second, clot formation was highly sensitive to TF patch location. Clots grew more rapidly when the TF patch was within the recirculation zone, particularly at the stagnation point, compared to patches located further downstream. This suggests that endothelial damage near disturbed flow zones (e.g., around stent struts) may pose a higher thrombosis risk. This is consistent with Taylor et al., who observed thrombus formation consistently in the low-wall shear stress region downstream of the step, extending into the recirculation zone[58]. The third observation is that clot growth dynamics depended on BFS steepness (round vs sharp-edged), with more pronounced growth in the sharp-edged configuration. This likely reflects the larger recirculation zone in the sharp-edged configuration. These combined models might be useful in optimizing stent strut design or develop plaque-shape specific risk profiles. In addition, these simulations could guide future in vitro flow experiments: currently our model predicts where the clot will form, guiding where to locate the TF patch and where to microscopically image clot formation.

Finally, the 2D stenosed geometry demonstrated that the upstream high-shear zone seemed to suppress fibrin clot formation. The model thus suggests that flow immediately downstream of a stenosis is more prone to fibrin clot formation. This is in agreement with literature: the downstream region of a stenosis is known to be thrombogenic in vitro[67]. This is largely attributed to the accumulation of coagulation factors in the recirculation zone that forms beyond the stenosis[68]. In proximal locations, the coagulation factors are more flushed away by the high shear rate upstream of the stenosis, limiting clot expansion. Furthermore, the plasma composition significantly affected clot growth. This shows that when the flow is applied, the implementation of plasma variations in modeling clot formation is of high importance.

The 3D simulations provide insights into the role of patient-specific vascular geometry in fibrin clot formation. Our results emphasise the significance of local morphological features, such as the low-shear region observed in Patient A, in facilitating fibrin retention. This finding aligns with clinical observations linking plaque ulceration, which creates low-shear areas, with increased thrombotic risk[69]. Conversely, Patient B's geometry lacked a prominent low-shear zone at the TF region, showed a slightly lower potential for coagulation initiation based on patient-specific blood data, and indeed showed minimal fibrin accumulation in our model. The insights from the 2D flow simulations further help to explain inter-patient differences in clot extent. For example, a small plaque rupture (i.e. small TF-patch size) located on the proximal side of a stenosis may experience high shear, limiting full fibrin clot growth and yield only a small mural fibrin-rich thrombus; whereas a large TF exposure area positioned within a downstream recirculation zone may overcome shear suppression, enabling formation of an occlusive fibrin-rich thrombus or embolus, potentially causing stroke. Note that as the current work isolates coagulation effects, the inclusion of platelet and RBC dynamics may alter the interpretation of thrombotic risk, especially in high-shear regions where platelet activation and aggregation promote thrombus formation[23]. In addition, while the simulated fibrin concentrations in the 3D simulations appeared modest, it is worth noting that in vivo, platelet adhesion and aggregation would likely contribute to initial patch sealing and promote fibrin retention by forming a local flow- barrier, thereby increasing the fibrin concentration[70,71].

The study acknowledges several limitations. In the current study, we report a single best-fit parameter set per patient without a formal identifiability analysis. Consequently, the fitted values should be interpreted as an assay-constrained parameterization that reproduces the observed TG phenotype, rather than as uniquely identifiable estimates. In addition, from a physiological standpoint, it is expected that parameters associated with normal coagulation lie between those of hypo- and hypercoagulable states. However, this ordering is not consistently observed for all fitted parameters (Table S2). These observations likely reflect two related factors. First, the model represents a highly reduced formulation of coagulation, meaning that individual parameters capture combined effects of multiple mechanisms rather than one-to-one biochemical processes. Second, correlations between parameters may allow different parameter combinations to reproduce the experimental TG curves with comparable accuracy. Therefore, the reported parameter sets should not be interpreted as unique and their

biochemical interpretation should be made with caution. However, we emphasize that the primary role of the fitted parameters in this work is predictive: they provide patient-specific inputs that drive the 1D and subsequent 2D/3D simulations toward individualized coagulation dynamics. Nevertheless, assessing the robustness of these predictions will require uncertainty quantification and identifiability analyses in future work.

Also, in the current model framework, patient-specific fitted reaction rates should be interpreted as effective parameters that represent the overall coagulation phenotype under the assay conditions, rather than as intrinsic biochemical reaction rates. Although inter-patient variability in TG is often driven by differences in coagulation factor concentrations, explicitly measuring and incorporating comprehensive patient-specific concentration panels is currently impractical, as this typically requires multiple specialized assays. From a translational perspective, inferring patient-specific kinetic rate parameters from a single TG assay is therefore more feasible than relying on extensive biochemical profiling. Moreover, previously discussed studies have shown that explicitly adjusting coagulation factor concentrations in more detailed models does not necessarily lead to accurate quantitative predictions in patient plasma, motivating our alternative approach based on kinetic-rate fitting[28,38]. In addition, similar data-driven calibration strategies have been reported previously. For example, Méndez et al. employed Bayesian inference to infer effective kinetic parameters from TG data, demonstrating good agreement with measured TG dynamics[60]. In later CFD-oriented work, the same group used this coagulation model in a more extensive thrombosis model, calibrated and validated this against in vitro experiments, and reported close agreement with thrombus evolution in calibrated 2D simulations[72].

Furthermore, the TG and thrombodynamics curves shown in this study are presented as representative examples, and replicate measurements on the same plasma samples were not available to quantify experiment-specific uncertainty. As a result, error bars are not shown. To place these results in context, reported repeatability of CAT-based thrombin generation assays indicates intra-assay variability below approximately 7.6% for key TG parameters in control plasma, depending on assay conditions and calibration[73,74]. Similarly, thrombodynamics measurements have been reported to exhibit low intra-laboratory variability, with coefficients of variation of approximately 2.4% for clot growth velocity[40]. While these values provide an estimate of typical experimental uncertainty, future studies including replicate measurements will be important for quantifying uncertainty at the individual sample level.

A numerical limitation of the present study is that we do not provide a dedicated mesh- and timestep-refinement analysis for the patient-specific 3D simulations. For the 2D benchmark geometries, spatial and temporal resolutions were adopted from Taylor et al., who performed sensitivity analyses for this type of reaction-transport thrombus modelling, and these settings were applied consistently across all 2D cases and the subsequent 3D simulations[58]. For the 3D simulations, the selected spatial resolution is consistent with prior numerical work on reaction–transport problems in 3D arterial geometries, in which an element size of 100 μm was shown to be sufficient, with errors below 2% compared to a finer 50 μm mesh[75]. While this provides supporting evidence for the chosen resolution, future work should include a systematic mesh- and timestep-refinement analysis for patient-specific 3D coagulation simulations to further strengthen quantitative robustness.

Although the model successfully captures coagulation and fibrin formation under flow, it does not account for platelet activation, aggregation, or RBC dynamics. Continuum modeling studies that include RBC transport and margination highlight how RBCs laterally displace platelets toward the vessel wall, enhancing platelet–wall interactions and locally increasing the concentrations of procoagulant factors[76,77]. Platelet aggregation, in turn, can form a physical plug that alters near-wall shear, creates flow stagnation zones, and provides additional binding sites for thrombin and fibrin. Especially in plaque rupture, early thrombus development is often governed by rapid, shear-dependent platelet adhesion and aggregation mediated by von Willebrand factor (vWF). Incorporating platelet–vWF dynamics would be expected to accelerate early thrombus growth under high-shear conditions[78], and to rapidly alter local hemodynamics and transport through thrombus-induced changes in shear gradients and near-wall flow[79]. Without these effects, the current model may underestimate the extent of fibrin accumulation. Future research should focus on integrating the present coagulation framework with (continuum) models of platelet[80], vWF[67], and RBC behaviour[77] to capture more complete thrombus dynamics. Although these critical hemostatic features are not implemented, it is worth noting that most computational studies of stenosed arteries have primarily focused on platelet activation and aggregation, and the role of vWF[67,81–84]. The present approach can be viewed as complementary to such platelet-centric frameworks. While it is less suited to platelet-dominated regimes, such as those under ultra-high shear conditions, it provides insights into situations where coagulation kinetics are expected to play a more prominent role, such as within slow-flow recirculation zones downstream of stenoses or in regions where large, TF–rich areas are exposed following plaque rupture. Furthermore, other important factors on the endothelium, such as protein C, should be implemented before applying such model in the in vivo situation. Nevertheless, as Belyaev et al. pointed out, unknown parameters and biological "mysteries", such as the precise role of certain feedback mechanisms, remain major challenges in coagulation modeling[35]. To address these uncertainties, incorporating data-driven approaches, such as the methodologies proposed by Link et al.[85], could help refine parameter estimation and improve model accuracy.

Conclusions

This study introduces a novel and unique unified workflow linking coagulation assays to multiscale, patient-specific in silico simulations. Parameters inferred from TG assays were validated against TD data and propagated into flow-resolved 2D and patient-specific 3D domains without further tuning. The framework reproduced key experimental trends and provided mechanistic insights into how plasma composition, TF exposure, and hemodynamics jointly determine fibrin formation. Overall, these results highlight the importance of integrating biochemical and hemodynamic factors to explain inter-individual differences in thrombotic risk. Further extending and validating this framework may ultimately enable predictive in silico studies of (athero)thrombosis to support individualized treatment strategies.

Data availability

The datasets generated during and/or analysed during the current study are available from the corresponding author on reasonable request.

Received: 14 November 2025; Accepted: 17 March 2026
Published online: 05 April 2026

References

1. Kuharsky, A. L. & Fogelson, A. L. Surface-mediated control of blood coagulation: the role of binding site densities and platelet deposition. *Biophys. J* . **80**, 1050–1074 (2001).
2. Bentzon, J. F., Otsuka, F., Virmani, R. & Falk, E. Mechanisms of plaque formation and rupture. *Circ. Res.* **114**, 1852–1866 (2014).
3. Libby, P., Pasterkamp, G., Crea, F. & Jang, I.-K. Reassessing the mechanisms of acute coronary syndromes: the "vulnerable plaque" and superficial erosion. *Circ. Res.* **124**, 150–160 (2019).
4. Kawai, K., Finn, A. V. & Virmani, R. Subclinical atherosclerosis: Part 1: What is it? can it be defined at the histological level?. *Arterioscler. Thromb. Vasc. Biol.* **44**, 12–23 (2024).
5. Sato, Y. et al. Proportion of fibrin and platelets differs in thrombi on ruptured and eroded coronary atherosclerotic plaques in humans. *Heart* **91**, 526–530 (2005).
6. Tatsumi, K. & Mackman, N. Tissue factor and atherothrombosis. *J. Atheroscler. Thromb.* **22**, 543–549 (2015).
7. Grover, S. P. & Mackman, N. Tissue factor in atherosclerosis and atherothrombosis. *Atherosclerosis* **307**, 80–86 (2020).
8. Sakariassen, K. S., Orning, L. & Turitto, V. T. The impact of blood shear rate on arterial thrombus formation. *Future Sci. OA***1**, FSO30 (2015).
9. Versteeg, H. H., Heemskerk, J. W., Levi, M. & Reitsma, P. H. New fundamentals in hemostasis. *Physiol. Rev.* **93**, 327–358 (2013).
10. Carcaillon, L. et al. Increased thrombin generation is associated with acute ischemic stroke but not with coronary heart disease in the elderly: the three-city cohort study. *Arterioscler. Thromb. Vasc. Biol.* **31**, 1445–1451 (2011).
11. Loeffen, R. et al. Associations between thrombin generation and the risk of cardiovascular disease in elderly patients: Results from the prosper study. *J. Gerontol. Ser. A Biomed. Sci. Med. Sci.* **70**, 982–988 (2015).
12. Hathcock, J. J. Flow effects on coagulation and thrombosis. *Arterioscler. Thromb. Vasc. Biol.* **26**, 1729–1737 (2006).
13. Leiderman, K. & Fogelson, A. L. Grow with the flow: A spatial-temporal model of platelet deposition and blood coagulation under flow. *Math. Med. Biol. J. IMA* **28**, 47–84 (2011).
14. Kim, O. V., Xu, Z., Rosen, E. D. & Alber, M. S. Fibrin networks regulate protein transport during thrombus development. *PLoS Comput. Biol.* **9**, e1003095 (2013).
15. Eyisoylu, H., Hazekamp, E. D., Cruts, J., Koenderink, G. H. & de Maat, M. P. Flow affects the structural and mechanical properties of the fibrin network in plasma clots. *J. Mater. Sci. - Mater. Med.* **35**, 8 (2024).
16. Govindarajan, V. et al. Impact of tissue factor localization on blood clot structure and resistance under venous shear. *Biophys. J* . **114**, 978–991 (2018).
17. Colace, T. V., Muthard, R. W. & Diamond, S. L. Thrombus growth and embolism on tissue factor-bearing collagen surfaces under flow: Role of thrombin with and without fibrin. *Arterioscler. Thromb. Vasc. Biol.* **32**, 1466–1476 (2012).
18. Falati, S., Gross, P., Merrill-Skoloff, G., Furie, B. C. & Furie, B. Real-time in vivo imaging of platelets, tissue factor and fibrin during arterial thrombus formation in the mouse (2002).
19. Shen, F., Kastrup, C. J., Liu, Y. & Ismagilov, R. F. Threshold response of initiation of blood coagulation by tissue factor in patterned microfluidic capillaries is controlled by shear rate. *Arterioscler. Thromb. Vasc. Biol.* **28**, 2035–2041 (2008).
20. Okorie, U. M., Denney, W. S., Chatterjee, M. S., Neeves, K. B. & Diamond, S. L. Determination of surface tissue factor thresholds that trigger coagulation at venous and arterial shear rates: amplification of 100 fm circulating tissue factor requires flow. *Blood J. Am. Soc. Hematol.* **111**, 3507–3513 (2008).
21. Fogelson, A. L. & Neeves, K. B. Fluid mechanics of blood clot formation. *Annu. Rev. Fluid Mech.* **47**, 377–403 (2015).
22. Yesudasan, S. & Averett, R. D. Recent advances in computational modeling of fibrin clot formation: A review. *Comput. Biol. Chem.* **83**, 107148 (2019).
23. Gutierrez, N. G., Mukherjee, D. & Bark, D. Jr. Decoding thrombosis through code: A review of computational models. *J. Thromb. Haemost.* **22**, 35–47 (2024).
24. Hockin, M. F., Jones, K. C., Everse, S. J. & Mann, K. G. A model for the stoichiometric regulation of blood coagulation. *J. Biol. Chem.* **277**, 18322–18333 (2002).
25. Wagenvoord, R., Hemker, P. & Hemker, H. The limits of simulation of the clotting system. *J. Thromb. Haemost.* **4**, 1331–1338 (2006).
26. Chatterjee, M. S., Denney, W. S., Jing, H. & Diamond, S. L. Systems biology of coagulation initiation: kinetics of thrombin generation in resting and activated human blood. *PLoS Comput. Biol.* **6**, e1000950 (2010).
27. Panteleev, M. A. et al. Spatial propagation and localization of blood coagulation are regulated by intrinsic and protein c pathways, respectively. *Biophys. J* . **90**, 1489–1500 (2006).
28. Kuprash, A. D. et al. Sensitivity and robustness of spatially dependent thrombin generation and fibrin clot propagation. *Biophys. J* . **115**, 2461–2473 (2018).
29. Kastrup, C. J., Shen, F., Runyon, M. K. & Ismagilov, R. F. Characterization of the threshold response of initiation of blood clotting to stimulus patch size. *Biophys. J* . **93**, 2969–2977 (2007).
30. Anand, M., Rajagopal, K. & Rajagopal, K. A model for the formation, growth, and lysis of clots in quiescent plasma. A comparison between the effects of antithrombin iii deficiency and protein c deficiency. *J. Theor. Biol.* **253**, 725–738 (2008).
31. Biscombe, C. J., Dower, S. K., Muir, I. L. & Harvie, D. J. Modeling thrombin generation in plasma under diffusion and flow. *Biophys. J* . **119**, 162–181 (2020).
32. Anand, M., Rajagopal, K. & Rajagopal, K. A model for the formation and lysis of blood clots. *Pathophysiol. Haemost. Thromb.* **34**, 109–120 (2006).
33. Bouchnita, A., Terekhov, K., Nony, P., Vassilevski, Y. & Volpert, V. A mathematical model to quantify the effects of platelet count, shear rate, and injury size on the initiation of blood coagulation under venous flow conditions. *PLoS ONE* **15**, e0235392 (2020).
34. Dydek, E. V. & Chaikof, E. L. Simulated thrombin generation in the presence of surface-bound heparin and circulating tissue factor. *Ann. Biomed. Eng.* **44**, 1072–1084 (2016).
35. Belyaev, A., Dunster, J. L., Gibbins, J. M., Panteleev, M. A. & Volpert, V. Modeling thrombosis in silico: Frontiers, challenges, unresolved problems and milestones. *Phys. Life Rev.* **26**, 57–95 (2018).
36. Owen, M. J. et al. Mathematical models of coagulation-are we there yet? *J. Thromb. Haemostasis* (2024).
37. Chelle, P. et al. Evaluation and calibration of in silico models of thrombin generation using experimental data from healthy and haemophilic subjects. *Bull. Math. Biol.* **80**, 1989–2025 (2018).
38. Pisaryuk, A. S., Povalyaev, N. M., Poletaev, A. V. & Shibeko, A. M. Systems biology approach for personalized hemostasis correction. *J. Pers. Med.* **12**, 1903 (2022).
39. Dashkevich, N. et al. Thrombin activity propagates in space during blood coagulation as an excitation wave. *Biophys. J* . **103**, 2233–2240 (2012).

40. Balandina, A. N. et al. Thrombodynamics-a new global hemostasis assay for heparin monitoring in patients under the anticoagulant treatment. *PLoS ONE* **13**, e0199900 (2018).
41. Calderara, D. B. et al. Hyper-coagulability in obese patients accurately identified by combinations of global coagulation assay parameters. *Thromb. Res.* **187**, 91–102 (2020).
42. Hemker, H., Kerdelo, S. & Kremers, R. Is there value in kinetic modeling of thrombin generation? no (unless...). *J. Thromb. Haemostasis* **10**, 1470–1477 (2012).
43. Ratto, N. et al. Patient-specific modelling of blood coagulation. *Bull. Math. Biol.* **83**, 1–31 (2021).
44. Hemker, H. et al. The calibrated automated thrombogram (CAT): A universal routine test for hyper-and hypocoagulability. *Pathophysiol. Haemost. Thromb.* **32**, 249–253 (2002).
45. Ratto, N., Tokarev, A., Chelle, P., Tardy-Poncet, B. & Volpert, V. Clustering of thrombin generation test data using a reduced mathematical model of blood coagulation. *Acta. Biotheor.* **68**, 21–43 (2020).
46. Panteleev, M. A., Balandina, A. N., Lipets, E. N., Ovanesov, M. V. & Ataullakhanov, F. I. Task-oriented modular decomposition of biological networks: Trigger mechanism in blood coagulation. *Biophys. J .* **98**, 1751–1761 (2010).
47. Quicken, S. et al. Application of an adaptive polynomial chaos expansion on computationally expensive three-dimensional cardiovascular models for uncertainty quantification and sensitivity analysis. *J. Biomech. Eng.* **138**, 121010 (2016).
48. Blatman, G. & Sudret, B. An adaptive algorithm to build up sparse polynomial chaos expansions for stochastic finite element analysis. *Probab. Eng. Mech.* **25**, 183–197 (2010).
49. Zhang, X.-Y., Trame, M. N., Lesko, L. J. & Schmidt, S. Sobol sensitivity analysis: A tool to guide the development and evaluation of systems pharmacology models. *CPT Pharmacometrics Syst. Pharmacol.* textbf4, 69–79 (2015).
50. Truijman, M. et al. Plaque at risk (parisk): Prospective multicenter study to improve diagnosis of high-risk carotid plaques. *Int. J. Stroke* **9**, 747–754 (2014).
51. Crombag, G. A. et al. No association between thrombin generation and intra-plaque haemorrhage in symptomatic carotid atherosclerotic plaques: the plaque at risk (parisk) study. *Thromb. Haemost.* **118**, 1461–1469 (2018).
52. Sequeira, A., Santos, R. F. & Bodnár, T. Blood coagulation dynamics: Mathematical modeling and stability results. *Math. Biosci. Eng.* **8**, 425–443 (2011).
53. Anand, M., Rajagopal, K. & Rajagopal, K. A model incorporating some of the mechanical and biochemical factors underlying clot formation and dissolution in flowing blood. *Comput. Math. Methods Med.* **5**, 183–218 (2003).
54. Bodnár, T. & Sequeira, A. Numerical simulation of the coagulation dynamics of blood. *Comput. Math. Methods Med.* **9**, 83–104 (2008).
55. Wufsus, A. R., Macera, N. & Neeves, K. The hydraulic permeability of blood clots as a function of fibrin and platelet density. *Biophys. J .* **104**, 1812–1823 (2013).
56. Weisel, J. W. & Litvinov, R. I. Mechanisms of fibrin polymerization and clinical implications. *Blood J. Am. Soc. Hematol.* **121**, 1712–1719 (2013).
57. Chernysh, I. N. & Weisel, J. W. Dynamic imaging of fibrin network formation correlated with other measures of polymerization. *Blood J. Am. Soc. Hematol.* **111**, 4854–4861 (2008).
58. Taylor, J. O., Meyer, R. S., Deutsch, S. & Manning, K. B. Development of a computational model for macroscopic predictions of device-induced thrombosis. *Biomech. Model. Mechanobiol.* **15**, 1713–1731 (2016).
59. Dilba, K. et al. The association between time-varying wall shear stress and the development of plaque ulcerations in carotid arteries from the plaque at risk study. *Front. Cardiovasc. Med.* **8**, 732646 (2021).
60. Méndez Rojano, R. et al. Sensitivity analysis and model reduction. Kinetics of the coagulation cascade including the contact activation system. *Biomech. Model. Mechanobiol.* **18**, 1139–1153 (2019).
61. Nelson, A. C., Kelley, M. A., Haynes, L. M. & Leiderman, K. Mathematical models of fibrin polymerization: Past, present, and future. *Curr. Opin. Biomed. Eng.* **20**, 100350 (2021).
62. Wolberg, A. S. & Campbell, R. A. Thrombin generation, fibrin clot formation and hemostasis. *Transfus. Apheres. Sci.* **38**, 15–23 (2008).
63. Undas, A., Slowik, A., Wolkow, P., Szczudlik, A. & Tracz, W. Fibrin clot properties in acute ischemic stroke: relation to neurological deficit. *Thromb. Res.* **125**, 357–361 (2010).
64. Lord, S. T. Molecular mechanisms affecting fibrin structure and stability. *Arterioscler. Thromb. Vasc. Biol.* **31**, 494–499 (2011).
65. Jordan, S. & Chaikof, E. Simulated surface-induced thrombin generation in a flow field. *Biophys. J .* **101**, 276–286 (2011).
66. Kastrup, C. J., Runyon, M. K., Shen, F. & Ismagilov, R. F. Modular chemical mechanism predicts spatiotemporal dynamics of initiation in the complex network of hemostasis. *Proc. Natl. Acad. Sci.* **103**, 15747–15752 (2006).
67. Westein, E. et al. Atherosclerotic geometries exacerbate pathological thrombus formation poststenosis in a von willebrand factor-dependent manner. *Proc. Natl. Acad. Sci.* **110**, 1357–1362 (2013).
68. Wootton, D. M. & Ku, D. N. Fluid mechanics of vascular systems, diseases, and thrombosis. *Annu. Rev. Biomed. Eng.* **1**, 299–329 (1999).
69. Rafailidis, V., Chryssogonidis, I., Tegos, T., Kouskouras, K. & Charitanti-Kouridou, A. Imaging of the ulcerated carotid atherosclerotic plaque: a review of the literature. *Insights Imaging* **8**, 213–225 (2017).
70. Brouns, S. L., Provenzale, I., van Geffen, J. P., van der Meijden, P. E. & Heemskerk, J. W. Localized endothelial-based control of platelet aggregation and coagulation under flow: A proof-of-principle vessel-on-a-chip study. *J. Thromb. Haemost.* **18**, 931–941 (2020).
71. Ruggeri, Z. M. Platelet adhesion under flow. *Microcirculation* **16**, 58–83 (2009).
72. Méndez Rojano, R. et al. A fibrin enhanced thrombosis model for medical devices operating at low shear regimes or large surface areas. *PLoS Comput. Biol.* **18**, e1010277 (2022).
73. Duarte, R. C. F. et al. Standardization and evaluation of the performance of the thrombin generation test under hypo-and hypercoagulability conditions. *Hematol. Transfus. Cell Ther.* **41**, 244–252 (2019).
74. Giesen, P. et al. Calibrated automated thrombogram II: Removing barriers for thrombin generation measurements. *Thromb. J.* **19**, 60 (2021).
75. Ten Have, A., Gijsen, F., Wentzel, J., Slager, C. & van der Steen, A. Temperature distribution in atherosclerotic coronary arteries: Influence of plaque geometry and flow (a numerical study). *Phys. Med. Biol.* **49**, 4447 (2004).
76. Mehrabadi, M., Ku, D. N. & Aidun, C. K. A continuum model for platelet transport in flowing blood based on direct numerical simulations of cellular blood flow. *Ann. Biomed. Eng.* **43**, 1410–1421 (2015).
77. Wu, W.-T., Aubry, N., Massoudi, M. & Antaki, J. F. Transport of platelets induced by red blood cells based on mixture theory. *Int. J. Eng. Sci.* **118**, 16–27 (2017).
78. Casa, L. D., Deaton, D. H. & Ku, D. N. Role of high shear rate in thrombosis. *J. Vasc. Surg.* **61**, 1068–1080 (2015).
79. Rana, A., Westein, E., Niego, B. & Hagemeyer, C. E. Shear-dependent platelet aggregation: Mechanisms and therapeutic opportunities. *Front. Cardiovasc. Med.* **6**, 141 (2019).
80. Rezaeimoghaddam, M. & van de Vosse, F. N. Continuum modeling of thrombus formation and growth under different shear rates. *J. Biomech.* **132**, 110915 (2022).
81. Du, J., Aspray, E. & Fogelson, A. Computational investigation of platelet thrombus mechanics and stability in stenotic channels. *J. Biomech.* **122**, 110398 (2021).
82. Casa, L. D. & Ku, D. N. Thrombus formation at high shear rates. *Annu. Rev. Biomed. Eng.* **19**, 415–433 (2017).

83. Wu, W.-T., Zhussupbekov, M., Aubry, N., Antaki, J. F. & Massoudi, M. Simulation of thrombosis in a stenotic microchannel: The effects of vwf-enhanced shear activation of platelets. *Int. J. Eng. Sci.* **147**, 103206 (2020).
84. Zhussupbekov, M., Méndez Rojano, R., Wu, W.-T., Massoudi, M. & Antaki, J. F. A continuum model for the unfolding of von Willebrand factor. *Ann. Biomed. Eng.* **49**, 2646–2658 (2021).
85. Link, K. G. et al. Computationally driven discovery in coagulation. *Arterioscler. Thromb. Vasc. Biol.* **41**, 79–86 (2021).

Acknowledgements
We are grateful to Inge Vangenechten and Emmy van Reusel for providing access to the necessary equipment and supporting the thrombodynamics experiments. We also thank Moniek de Maat for insightful discussions about the coagulation cascade and the in vitro setups. We appreciate the help of Ton Lisman for sharing thrombin generation and thrombodynamics data for the initial 1D model development. Furthermore, we thank Henri Spronk, Daniel Bos, and Eline Kooij for providing data from the PARISK-study. We would also like to thank Sjeng Quicken for the assistance in performing the model sensitivity analysis. This work used the Dutch national e-infrastructure with the support of the SURF Cooperative using grant no. EINF-12214. The authors acknowledge the EU funded project In Silico World, grant number 101016503. The authors further acknowledge the partnership with Ansys.

Author contributions
J.C. conceptualization, methodology, software, data curation, formal analysis, investigation, writing. M.R. conceptualization, supervision, investigation. A.R. conceptualization, software, formal analysis. L.B. investigation. R.A. conceptualization. F.V. conceptualization, methodology, supervision. F.G. conceptualization, methodology, funding acquisition, supervision. All authors reviewed the manuscript.

Declarations

Competing interests
The authors declare no competing interests.

Additional information
Supplementary Information The online version contains supplementary material available at https://doi.org/10.1038/s41598-026-45247-0.

Correspondence and requests for materials should be addressed to F.J.H.G.

Reprints and permissions information is available at www.nature.com/reprints.

Publisher's note Springer Nature remains neutral with regard to jurisdictional claims in published maps and institutional affiliations.